Lectins enhance SARS-CoV-2 infection and influence neutralizing antibodies

https://doi.org/10.1038/s41586-021-03925-1

Received: 3 April 2021

Accepted: 18 August 2021

Published online: 31 August 2021

Check for updates

Florian A. Lempp[1], Leah B. Soriaga[1], Martin Montiel-Ruiz[1], Fabio Benigni[2], Julia Noack[1], Young-Jun Park[3], Siro Bianchi[2], Alexandra C. Walls[3], John E. Bowen[3], Jiayi Zhou[1], Hannah Kaiser[1], Anshu Joshi[3], Maria Agostini[1], Marcel Meury[1], Exequiel Dellota Jr[1], Stefano Jaconi[2], Elisabetta Cameroni[2], Javier Martinez-Picado[4,5,6], Júlia Vergara-Alert[7], Nuria Izquierdo-Useros[4,8], Herbert W. Virgin[1,9,10], Antonio Lanzavecchia[2], David Veesler[3], Lisa A. Purcell[11], Amalio Telenti[1,12] ✉ & Davide Corti[2,12] ✉

SARS-CoV-2 infection—which involves both cell attachment and membrane fusion—relies on the angiotensin-converting enzyme 2 (ACE2) receptor, which is paradoxically found at low levels in the respiratory tract[1–3], suggesting that there may be additional mechanisms facilitating infection. Here we show that C-type lectin receptors, DC-SIGN, L-SIGN and the sialic acid–binding immunoglobulin-like lectin 1 (SIGLEC1) function as attachment receptors by enhancing ACE2-mediated infection and modulating the neutralizing activity of different classes of spike-specific antibodies. Antibodies to the amino-terminal domain or to the conserved site at the base of the receptor-binding domain, while poorly neutralizing infection of ACE2-overexpressing cells, effectively block lectin-facilitated infection. Conversely, antibodies to the receptor binding motif, while potently neutralizing infection of ACE2-overexpressing cells, poorly neutralize infection of cells expressing DC-SIGN or L-SIGN and trigger fusogenic rearrangement of the spike, promoting cell-to-cell fusion. Collectively, these findings identify a lectin-dependent pathway that enhances ACE2-dependent infection by SARS-CoV-2 and reveal distinct mechanisms of neutralization by different classes of spike-specific antibodies.

SARS-CoV-2 infects target cells via the spike (S) glycoprotein, which is organized as a homotrimer with each monomer comprising S1 and S2 subunits[4]. The infection process includes binding to cells, triggering of conformational changes in S and then fusion of the viral envelope with the target cell membrane. The S1 subunit of S comprises the N-terminal domain (NTD) and the receptor binding domain (RBD). The RBD interacts with ACE2 through a region defined as the receptor binding motif (RBM). Antibodies against the RBD contribute the majority of the neutralizing activity of polyclonal serum antibodies[5,6], potently neutralize SARS-CoV-2 in vitro[7,8] and have shown efficacy in clinical trials for prophylaxis and early therapy of COVID-19[9,10].

The search for SARS-CoV-2-neutralizing antibodies has been facilitated by the use of target cells overexpressing the ACE2 receptor[11]. However, ACE2 expression in the lower respiratory tract is limited, with low levels found in only a small number of type II alveolar basal, goblet and mucous cells[1–3]. The paradox of low ACE2 levels in the lung and infection in other tissues leading to extrapulmonary complications[12] raises the possibility that additional receptors may contribute to viral infection and dissemination, such as DC-SIGN (also known as CD209), L-SIGN (also known as CD209L or CLEC4M), neuropilin-1 (NRP-1), basigin (also known as CD147) or heparan sulfate[13–17]. It remains to be established whether these molecules act as alternative primary receptors for viral entry, as co-receptors or as attachment receptors that tether viral particles, enhancing their interaction with ACE2.

In this study, we identify DC-SIGN, L-SIGN and SIGLEC1 (also known as CD169, sialoadhesin or Siglec-1) as attachment receptors that enhance ACE2-dependent infection and demonstrate different mechanisms of neutralization by antibodies targeting RBM and non-RBM sites in the presence or absence of lectins.

Lectins are attachment receptors for SARS-CoV-2

To develop an assay for identification of attachment receptors of SARS-CoV-2 infection, we used HEK 293T cells that express low endogenous levels of ACE2. HEK 293T cells were transfected with vectors encoding ACE2 or one of 13 selected lectins and published receptor candidates before infection with vesicular stomatitis virus (VSV) SARS-CoV-2 pseudovirus. Untransfected HEK 293T cells were only weakly permissive to infection, and ACE2 overexpression led to a marked increase in pseudovirus entry. Increased infectivity was also observed in HEK 293T cells following transfection with C-type lectins DC-SIGN and L-SIGN, which were previously reported to be entry

[1]Vir Biotechnology, San Francisco, CA, USA. [2]Humabs Biomed SA, a subsidiary of Vir Biotechnology, Bellinzona, Switzerland. [3]Department of Biochemistry, University of Washington, Seattle, WA, USA. [4]IrsiCaixa AIDS Research Institute, Badalona, Spain. [5]University of Vic–Central University of Catalonia (UVic-UCC), Vic, Spain. [6]Catalan Institution for Research and Advanced Studies (ICREA), Barcelona, Spain. [7]IRTA, Centre de Recerca en Sanitat Animal (CReSA, IRTA-UAB), Campus de la UAB, Bellaterra (Cerdanyola del Vallès), Spain. [8]Germans Trias i Pujol Research Institute (IGTP), Can Ruti Campus, Badalona, Spain. [9]Department of Pathology and Immunology, Washington University School of Medicine, Saint Louis, MO, USA. [10]Department of Internal Medicine, UT Southwestern Medical Center, Dallas, TX, USA. [11]Vir Biotechnology, St Louis, MO, USA. [12]These authors contributed equally: Amalio Telenti, Davide Corti. ✉e-mail: atelenti@vir.bio; dcorti@vir.bio

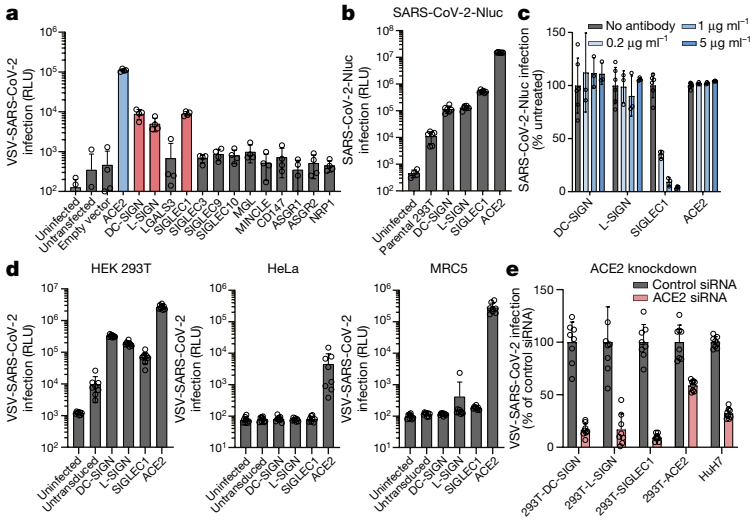

Fig. 1 | DC-SIGN, L-SIGN and SIGLEC1 function as attachment receptors for SARS-CoV-2 infection. a, VSV-SARS-CoV-2 infection of HEK 293T cells transfected to express ACE2 or a panel of selected lectins or candidate receptors ($n = 4$ biologically independent replicates). RLU, relative luminescence units. **b**, Stable cell lines were infected with SARS-CoV-2-Nluc and luciferase levels were quantified at 24 h ($n = 6$). **c**, Inhibition of SARS-CoV-2-Nluc infection with anti-SIGLEC1 monoclonal antibody (clone 7-239) ($n = 3$). **d**, Indicated cell lines were transduced to express lectins or ACE2 and infected with VSV-SARS-CoV-2 ($n = 8$). **e**, Effect of ACE2 siRNA transfection on infection with VSV-SARS-CoV-2 ($n = 8$).

receptors[13,14,18], as well as with SIGLEC1, which was not previously shown to mediate SARS-CoV-2 entry (Fig. 1a). NRP-1 and CD147 did not enhance SARS-CoV-2 infection in these conditions, although they have been suggested to act as entry receptors[15,16]. The infection-enhancing activity of the three lectins was also observed with authentic SARS-CoV-2 on cell lines stably expressing these factors (Fig. 1b, Extended Data Fig. 1a–d). A SIGLEC1-blocking antibody inhibited infection of SIGLEC1-expressing HEK 293T cells, supporting a role of this molecule as a SARS-CoV-2 co-factor (Fig. 1c).

The ectopic expression of DC-SIGN, L-SIGN and SIGLEC1 did not support infection of ACE2-negative cells, such as HeLa or MRC-5 cells (Fig. 1d), indicating that these lectins do not act as primary entry receptors. The requirement of ACE2 for viral infection of lectin-expressing cells was also demonstrated using ACE2-blocking antibodies or ACE2 small interfering RNA (siRNA) (Fig. 1e, Extended Data Fig. 1e).

Collectively, these data reveal a lectin-facilitated pathway of infection that is evident in cells expressing low levels of ACE2, supporting the notion that SARS-CoV-2 may use these lectins as attachment receptors to tether viral particles, thereby facilitating interaction with ACE2.

Attachment receptors facilitate *trans* infection

Interaction with ACE2 could take place in *cis* or in *trans*, as reported for HIV-1[19]. To address whether ACE2 and lectins can be found on the same cells (that is, in *cis*), we interrogated the lung cell atlas[20] (Extended Data Fig. 2a). DC-SIGN is expressed most prominently on IGSF21$^+$ dendritic cells, L-SIGN has a limited expression on vascular structures and SIGLEC1 is broadly expressed at the surface of alveolar macrophages, dendritic cells and monocytes. ACE2 expression is limited to subsets of alveolar epithelial type-2, basal and goblet cells. We then mined single-cell transcriptomic data on 3,085 lung epithelial and immune cells obtained from bronchoalveolar lavage (BAL) fluid or sputum of individuals who suffered from severe COVID-19[21]. The distribution of viral RNA per cell varied across annotated cell types. Specifically, the content of viral RNA in macrophages was greater relative to secretory cells ($P < 2.2 \times 10^{-16}$) (Extended Data Fig. 2b). SIGLEC1 was expressed in 41.4% (459 out of 1,107 cells) of SARS-CoV-2$^+$ macrophages, whereas ACE2 expression was negligible in these cells (Fig. 2a). Conversely, ACE2 expression was found in 10.6% (60 out of 565 cells) of SARS-CoV-2$^+$ secretory cells, whereas SIGLEC1 expression was negligible. In the full dataset (including cells from BAL or sputum without detectable SARS-CoV-2), 1,037 cells were annotated as dendritic cells (DCs), out of which 349 (34.6%) were SIGLEC1$^+$ (34.6%). In total, 19 out of 1,037 DCs (less than 2%) had detectable SARS-CoV-2, of which 47% (9 out of 19) exhibited detectable SIGLEC1 expression. Plotting SIGLEC1, DC-SIGN and L-SIGN expression as a function of SARS-CoV-2 viral load revealed a strong positive correlation for SIGLEC1 in macrophages (Fig. 2a). We confirmed this association in a separate transcriptomic dataset of 1,072 SARS-CoV-2$^+$ BAL cells from individuals with severe COVID-19[22]. We inspected the available sequenced reads from this dataset to assess the nature of viral RNA in SARS-CoV-2$^+$ BAL cells. Minimal viral replication was occurring in this cell population comprising largely of macrophages and other non-epithelial cell types.

The above results suggest limited cooperation of ACE2 and SIGLEC1 in *cis*, because these receptors are rarely expressed in the same cell, suggesting a role for *trans* infection from SIGLEC1$^+$ myeloid antigen presenting cells to ACE2$^+$ cells. Indeed, lectin-transduced HeLa cells showed enhanced capacity to promote VSV-SARS-CoV-2 *trans* infection of susceptible Vero E6-TMPRSS2 target cells (Fig. 2b), and SIGLEC1-mediated *trans* infection was inhibited by SIGLEC1-blocking antibodies (Fig. 2c, Extended Data Fig. 2c).

Next, we evaluated viral attachment and *trans* infection in primary myeloid cells using replication-competent SARS-CoV-2. Lectins are expressed mostly on antigen-presenting cells such as macrophages, DCs and monocytes, and their expression can be upregulated by innate inflammatory stimuli such as interferons[19]. While both macrophages and DCs are able to take up SARS-CoV-2 via SIGLEC1[23], macrophages mostly release inflammatory cytokines upon viral sensing[23,24]. Here we demonstrate that SIGLEC1 acts as a key factor in the *trans* infection of susceptible cells from primary DCs. In particular, we found that primary activated DCs cannot be productively infected but can mediate SARS-CoV-2 infection of target cells expressing ACE2 and TMPRSS2, and that this infection was reduced in the presence of an anti-SIGLEC1 antibody (Fig. 2d). In vivo, the *trans* infection mediated by SIGLEC1 could be relevant once inflammatory DCs migrate to pulmonary tissues upon SARS-CoV-2 infection and could help to spread infection in the lung and to distant tissues. These results are consistent with a role of lectins in dissemination of SARS-CoV-2.

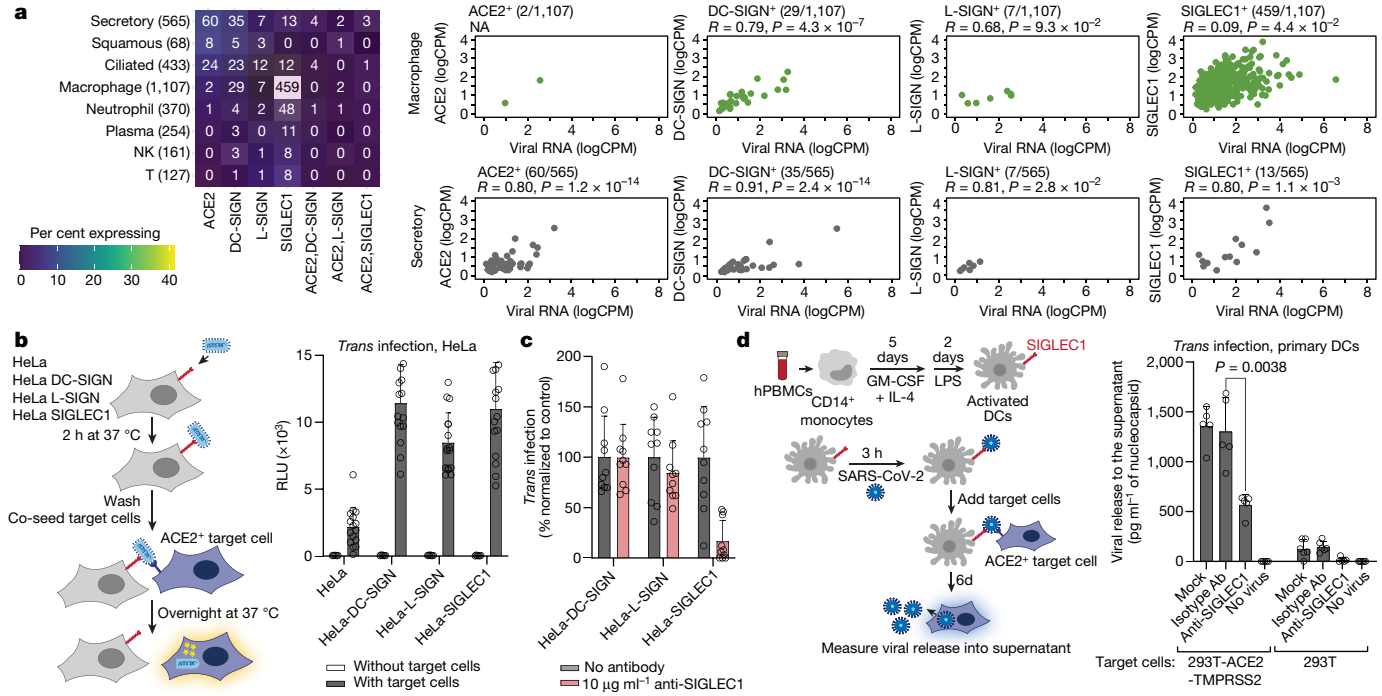

Fig. 2 | Expression of attachment receptors in infected tissues and their role in mediating *trans* infection. a, Left, heat map matrix showing counts of cells with detected transcripts for receptor gene(s) (*x*-axis) by SARS-CoV-2$^+$ cell type (*y*-axis) ($n = 3{,}085$ cells; total number of each cell type in parentheses). Right, correlation of receptor transcript counts with SARS-CoV-2 RNA counts in macrophages and secretory cells (transcript-positive cells shown as fraction of total number of cells of that type). Two-sided correlation test is based on counts (before log transformation) from Ren et al.[21]. NK, natural killer cells. CPM, counts per million transcripts; NA, not applicable. **b**, HeLa cells (grey) transduced with lectins (red) were incubated with VSV-SARS-CoV-2 (blue), washed and co-cultured with VeroE6-TMPRSS2 target cells. Infection (RLU) was assayed in the presence or absence of target cells (purple) ($n = 16$ biologically independent replicates). **c**, *Trans* infection performed as in **b**. Viral adsorption was performed in the presence of an anti-SIGLEC1 antibody ($n = 10$). **d**, Transmission of replication-competent SARS-CoV-2 by lipopolysaccharide (LPS)-activated DCs to susceptible target cells. Cells were pre-incubated with the indicated monoclonal antibodies, exposed to SARS-CoV-2, washed and incubated with indicated target HEK 293T cells. *Trans* infection was measured six days later as viral release in the supernatant. GM-CSF, granulocyte-macrophage colony-stimulating factor; hPBMCs, human peripheral blood mononuclear cells. Data are mean ± s.d. from two independent experiments including cells from five donors. Two-sided paired *t*-test.

Overexpression of ACE2 impairs neutralization

To investigate how ACE2 and attachment receptor expression levels influence neutralizing activity, we compared three monoclonal antibodies targeting distinct sites on the S protein: (1) S2E12, targeting the RBM site Ia/class 1 in the RBD[7]; (2) S309, targeting the conserved *N*-glycan-containing site IV/class 3 distal from RBM[25]; and (3) S2X333, targeting site i in the NTD[26] (Fig. 3a). These monoclonal antibodies completely neutralize infection of Vero E6 cells with authentic SARS-CoV-2, albeit with different potencies, and their activity was not influenced by the expression of the TMPRSS2 protease (Extended Data Fig. 3a, b). To understand the influence of receptor expression on neutralization, we used cell lines expressing ACE2 and TMPRSS2 (endogenously or upon transduction) at levels varying more than 1,000-fold (Fig. 3b, Extended Data Fig. 3c, d). Whereas the RBM monoclonal antibody S2E12 showed comparable neutralizing activity on all target cells, both S309 and S2X333 showed impaired neutralizing activity when tested on cells overexpressing ACE2, in terms of both maximal neutralization and potency (Fig. 3c, d). Similar results were obtained with both VSV-SARS-CoV-2 and authentic SARS-CoV-2-Nluc, a nanoluciferase-expressing infectious SARS-CoV-2 clone. Overall, a negative correlation was found between ACE2 levels and neutralization potency for non-RBM monoclonal antibodies (Extended Data Fig. 3e).

Given this uncertainty in the most relevant in vitro correlates of protection, we investigated the capacity of hamsterized S309 and S2E12 monoclonal antibodies to prevent SARS-CoV-2 infection in Syrian hamsters, an animal model that relies on endogenous expression of ACE2[27]. In a prophylactic setting, S309 was highly effective at doses as low as 0.4 mg kg^{-1} in terms of reduction of viral RNA and infectious virus levels and histopathological score in the lungs (Extended Data Fig. 4a). Furthermore, we did not observe substantial increased efficacy by co-administering S309 with an equal amount of the potent RBM S2E12 monoclonal antibody (Extended Data Fig. 4b). An 'Fc-silenced' version of hamsterized S309 monoclonal antibody (GH-S309-N297A) (Extended Data Fig. 5) was similarly protective against SARS-CoV-2 challenge of hamsters, underscoring that the neutralizing activity of S309 was the primary mechanism of action in this condition.

Together, these data indicate that neutralization assays using cells overexpressing ACE2 underestimate the neutralizing activity of non-RBM monoclonal antibodies, which are similarly protective in a relevant animal model of infection to RBM monoclonal antibodies[28]. The importance of this finding is also supported by the efficacy data of VIR-7831 (a derivative monoclonal antibody of S309) in a phase 3 clinical trial demonstrating 85% protection against hospitalization and death due to COVID-19[29].

Antibody-mediated membrane fusion

Infection of permissive cells involves both interactions with ACE2 and attachment receptors as well as fusion of the viral membrane to cellular membranes. We investigated how different classes of S-specific antibodies may interfere with viral fusion events that are involved in viral entry, but also in cell-to-cell fusion, leading to the formation of syncytia

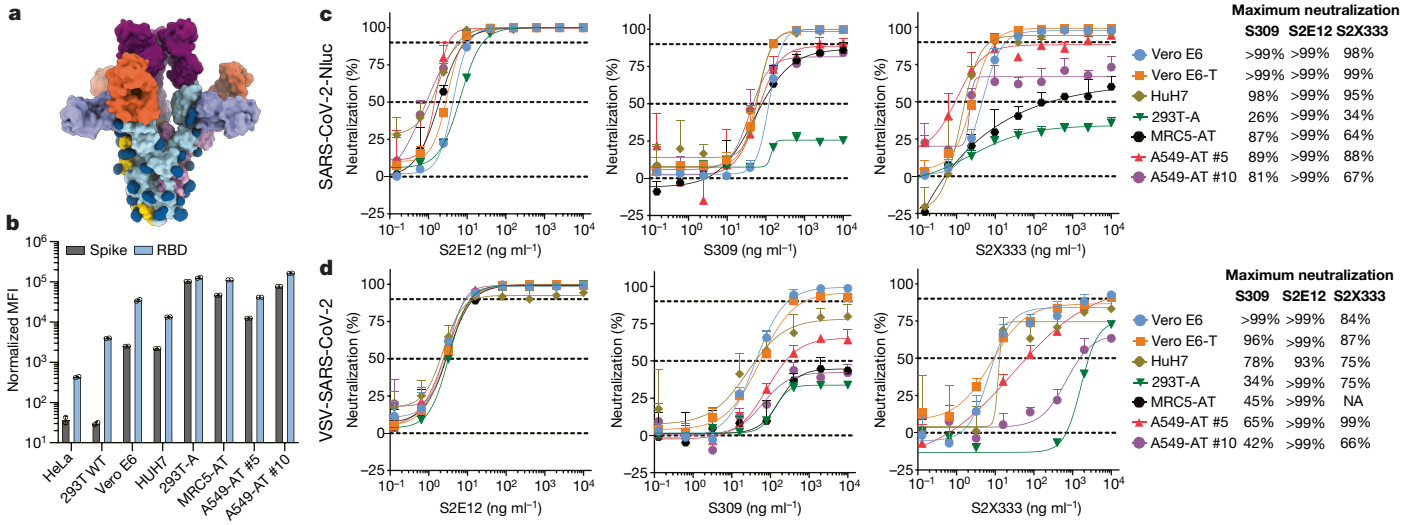

Fig. 3 | ACE2 overexpression influences neutralization by different classes of monoclonal antibodies. a, Surface rendering of a composite model of SARS-CoV-2 S bound to S309 (purple), S2E12 (magenta) and S2X333 (orange)[7,25,26]. The three SARS-CoV-2 S protomers are coloured light blue, gold and pink with *N*-linked glycans rendered dark blue. **b**, SARS-CoV-2 S or RBD binding to the indicated cell lines was quantified by flow cytometry. A, ACE2; T, TMPRSS2. Graph shows mean of two biological replicates. MFI, mean fluorescence intensity. **c**, **d**, A panel of seven cell lines was infected with SARS-CoV-2-Nluc (**c**) or VSV-SARS-CoV-2 pseudovirus (**d**) in the presence of S309, S2E12 or S2X333. Luciferase signals were quantified 24 h after infection ($n = 3$ biologically independent replicates).

in vitro[30] and multinucleate giant cells in human lung from infected individuals[31]. RBM-specific SARS-CoV neutralizing monoclonal antibodies can act as ACE2 mimics, triggering the fusogenic rearrangement of the S protein[32]. We evaluated monoclonal antibodies of different epitope specificity (Extended Data Table 1) to induce fusogenic rearrangement of soluble S trimers as measured by negative-stain electron microscopy imaging using Fab fragments of the respective monoclonal antibodies (Extended Data Fig. 6a). Five RBM monoclonal antibodies triggered rearrangement to the post-fusion state of a native SARS-CoV-2 S ectodomain trimer, probably owing to conformational selection of open RBDs. Most of these monoclonal antibodies triggered a rapid rearrangement of S, whereas S2D106 did so more slowly. As expected, S2M11, a RBM monoclonal antibody that locks neighbouring RBDs in a closed state[7], did not induce fusogenic S rearrangements. Antibodies to NTD (S2X333), to site Ib on RBD (REGN10987 and LyCoV555) or to the *N*-glycan-containing site at the base of RBD (S309) also did not trigger rearrangement, owing to the absence of conformational selection for open RBDs.

To investigate whether the antibody-mediated triggering of fusogenic rearrangement could promote membrane fusion, we evaluated a panel of monoclonal antibodies for their capacity to induce cell–cell fusion of CHO cells (which lack ACE2 expression) stably transduced with full-length SARS-CoV-2 S. Syncytia formation was triggered by all monoclonal antibodies recognizing antigenic sites Ia and IIa (Extended Data Table 1), which are accessible only in the open RBD state, with half-maximum effective concentration (EC_{50}) values ranging from 20 ng ml^{-1} for S2E12 to more than 1 μg ml^{-1} for S2D106 (Extended Data Fig. 6b–d). Syncytia were also formed by the three clinical-stage monoclonal antibodies: REGN10933 (casirivimab), Ly-CoV016 (etesevimab) and CT-P59 (regdanvimab). By contrast, syncytia were not formed in the presence of monoclonal antibodies binding to the open and closed RBD states (S2M11, S309, Ly-CoV555 (bamlanivimab) and REGN10987 (imdevimab)), to the NTD (S2X333) or to a conserved site in the S2 subunit stem helix (S2P6)[33]. A notable exception is provided by S2X58[34], a monoclonal antibody that was structurally defined in this study as binding to site Ib, which is accessible on open and closed RBDs (Extended Data Fig. 7). Of note, syncytia were also formed when using S2E12 Fab, indicating that cell–cell fusion does not result solely from cross-linking of S expressed on opposing cells (Extended Data Fig. 6g). Regarding the possible interaction between fusogenic and non-fusogenic antibodies, we found that syncytia formation induced by S2E12 could be inhibited by different classes of antibodies comprising S2M11 (which locks RBDs in a closed state), S309 (which targets an *N*-glycan-containing site at the base of RBD) and S2P6 (which destabilizes the stem helix in S2) (Extended Data Fig. 6e). These results highlight that different combinations of antibodies may interfere with each other by promoting or inhibiting membrane fusion.

To address whether antibodies may promote cell-to-cell spread of the infection, we co-cultured S-positive CHO cells with S-negative fluorescently labelled CHO cells. In these conditions, S2E12 promoted unidirectional fusion of S-positive CHO cells with S-negative CHO cells in the absence of ACE2 (defined here as '*trans* fusion') (Extended Data Fig. 6f). To address whether this mechanism may also mediate ACE2-independent infection of tethered virus, we infected HeLa-DC-SIGN cells with live SARS-CoV-2-Nluc virus in the presence of fusion-enhancing monoclonal antibodies at different dilutions. In these conditions, S2E12, S2D106 and S2X58 did not promote infection (Extended Data Fig. 8a). Collectively, these findings indicate that in certain conditions of antibody concentration and cell–cell proximity, a subclass of RBM antibodies selective for the open conformation of RBD may promote cell–cell fusion with ACE2-negative cells. However, the fusogenic activity of these monoclonal antibodies may not be sufficient to promote entry of virions tethered to the cell surface in the absence of ACE2. It remains to be established whether RBM monoclonal antibodies may mediate ACE2-independent SARS-CoV-2 entry under other conditions, as previously observed for anti-MERS-CoV neutralizing monoclonal antibodies captured by FcγRIIa-expressing cells in vitro[35].

Lectin receptors modulate neutralization

Given the dual function of certain RBM antibodies in inhibiting ACE2 binding and triggering fusion and the dependence on attachment receptor expression of neutralization by specific antibodies, we compared the neutralizing activity of a panel of monoclonal antibodies using authentic SARS-CoV-2 and target cells expressing different levels of ACE2 and lectin receptors. When tested on cells overexpressing ACE2, all anti-RBM monoclonal antibodies potently neutralized

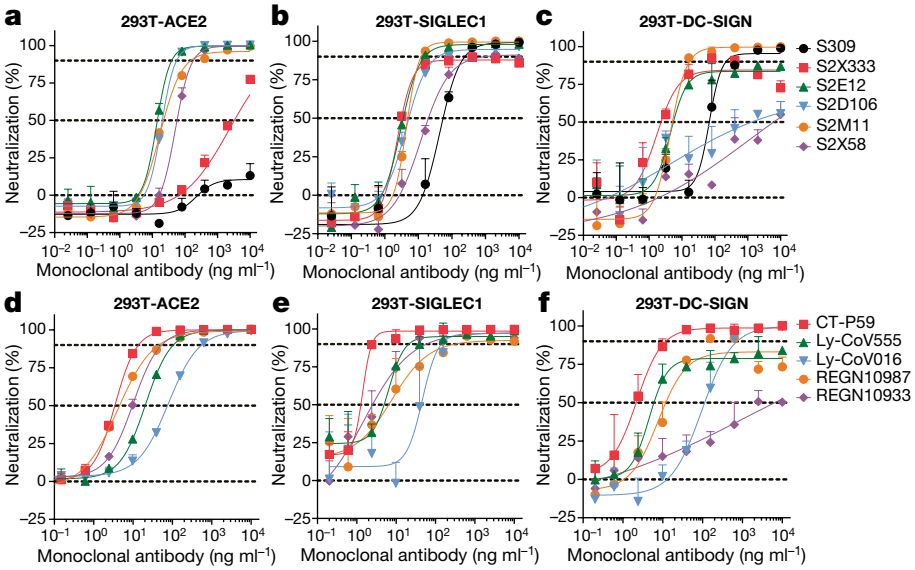

Fig. 4 | SIGLEC1, DC-SIGN and L-SIGN modulate neutralization by different classes of antibodies. a–**f**, Neutralization of infection with SARS-CoV-2-Nluc pre-incubated with indicated monoclonal antibodies on HEK 293T cell lines stably overexpressing lectins or ACE2. Infection was measured by luciferase signal 24 h after infection ($n = 3$ biologically independent replicates).

infection, whereas the non-RBM monoclonal antibodies S309 and S2X333 did not (Figs. 3, 4a, d). However, when tested on cells expressing low levels of ACE2 together with SIGLEC1, DC-SIGN or L-SIGN, S309 and S2X333 showed enhanced neutralizing activity, with S309 reaching 100% of neutralization. Of note, while all RBM monoclonal antibodies retained neutralizing activity on SIGLEC1$^+$ cells, several RBM monoclonal antibodies (S2D106, S2X58, REGN10987, REGN10933 and LyCoV555) lost neutralizing activity on cells expressing DC-SIGN or L-SIGN, showing only partial neutralization at the highest concentrations tested (Fig. 4b, c, e, f, Extended Data Fig. 8c–e). The loss of neutralizing activity of S2X58 and S2D106 monoclonal antibodies observed on DC-SIGN- and L-SIGN-expressing cells was confirmed with both replication-competent SARS-CoV-2 (wild type), as well as with live SARS-CoV-2-Nluc (Extended Data Fig. 8d). However, all neutralizing monoclonal antibodies blocked *trans* infection of Vero-E6-TMPRSS2 target cells from HeLa cells expressing either DC-SIGN or SIGLEC1 (Extended Data Fig. 9). Together, these data delineate a complex pattern of neutralization of *cis* or *trans* viral infection by different classes of monoclonal antibodies whereby the epitope specificity, valency of binding and the ability to trigger fusogenic rearrangement can result in differential blocking efficiency.

Discussion

We have shown that transmembrane lectins act as attachment receptors rather than entry receptors for SARS-CoV-2[13,14], thus facilitating infection via the canonical ACE2 pathway. This finding addresses the efficiency of lower respiratory tract infection despite the paradoxically low level of ACE2 expression, even in the presence of interferon[36,37]. The attachment role of lectins in SARS-CoV-2 infection is in line with the known biology of these adhesion molecules, which bind *N*-glycans characteristic of cellular membranes and pathogen surfaces to promote *trans* infection[38]. SIGLEC1 is of particular relevance because it is prominent in lung myeloid cells in association with viral RNA, thus supporting a model of *trans* infection, tissue dissemination and the triggering of immune responses by myeloid cells, rather than these cells being a direct target for productive infection[39]. Animal models also support a role of attachment receptors in viral pathogenesis[40,41].

Expression of lectin receptors influences the neutralizing activity of different classes of S-specific monoclonal antibodies. In addition, we have observed that various monoclonal antibodies have the ability to interfere with fusion events. We have expanded our initial observation on SARS-CoV and MERS-CoV[32,35] by showing that most RBM monoclonal antibodies can trigger the fusogenic rearrangement of S, albeit with varying efficiency. By stabilizing the RBDs in the open conformations, these antibodies might act as receptor mimics. This finding suggests that premature conformational triggering resulting in loss of the potential of a S protein to engender productive infection—we term this mechanism spike inactivation—may be the prominent mode of viral neutralization for this class of antibodies. However, we have also shown that these antibodies can promote fusion of S-expressing cells with neighbouring cells, even if the neighbouring cells lack ACE2. These data are consistent with a recent study reporting that a subset of RBM monoclonal antibodies can enhance S-mediated membrane fusion and formation of syncytia[42]. Notably, the formation of syncytia has been observed in authoptic samples from severe cases of COVID-19[31,43,44]. It is tempting to speculate that fusogenic antibodies, although highly effective[9,10], may contribute at a later stage to the spread of infection and inflammation.

Overall, our study highlights the finding that ranking of SARS-CoV-2-neutralizing antibodies is highly dependent on the level of ACE2 expression and on the presence of attachment receptors and identifies a mechanism that could result in the creation of multinucleate viral factories, potentially enhanced by specific antibodies.

Online content

Any methods, additional references, Nature Research reporting summaries, source data, extended data, supplementary information, acknowledgements, peer review information; details of author contributions and competing interests; and statements of data and code availability are available at https://doi.org/10.1038/s41586-021-03925-1.

1. Hikmet, F. et al. The protein expression profile of ACE2 in human tissues. *Mol. Syst. Biol.* **16**, e9610 (2020).
2. Hou, Y. J. et al. SARS-CoV-2 reverse genetics reveals a variable infection gradient in the respiratory tract. *Cell* **182**, 429–446.e14 (2020).
3. Zou, X. et al. Single-cell RNA-seq data analysis on the receptor ACE2 expression reveals the potential risk of different human organs vulnerable to 2019-nCoV infection. *Front. Med.* **14**, 185–192 (2020).

4. Walls, A. C. et al. Structure, function, and antigenicity of the SARS-CoV-2 spike glycoprotein. *Cell* **181**, 281–292.e6 (2020).
5. Piccoli, L. et al. Mapping neutralizing and immunodominant sites on the SARS-CoV-2 spike receptor-binding domain by structure-guided high-resolution serology. *Cell* **183**, 1024–1042.e21 (2020).
6. Greaney, A. J. et al. Comprehensive mapping of mutations to the SARS-CoV-2 receptor-binding domain that affect recognition by polyclonal human serum antibodies. *Cell Host Microbe* **29**, 463–476 (2021).
7. Tortorici, M. A. et al. Ultrapotent human antibodies protect against SARS-CoV-2 challenge via multiple mechanisms. *Science* **370**, 950–957 (2020).
8. Hansen, J. et al. Studies in humanized mice and convalescent humans yield a SARS-CoV-2 antibody cocktail. *Science* **369**, 1010–1014 (2020).
9. Chen, P. et al. SARS-CoV-2 neutralizing antibody LY-CoV555 in outpatients with Covid-19. *N. Engl. J. Med.* **384**, 229–237 (2021).
10. Weinreich, D. M. et al. REGN-COV2, a neutralizing antibody cocktail, in outpatients with Covid-19. *N. Engl. J. Med.* **384**, 238–251 (2021).
11. Crawford, K. H. D. et al. Protocol and reagents for pseudotyping lentiviral particles with SARS-CoV-2 spike protein for neutralization assays. *Viruses* **12**, 238 (2020).
12. Gustine, J. N. & Jones, D. Immunopathology of hyperinflammation in COVID-19. *Am. J. Pathol.* **191**, 4–17 (2021).
13. Amraie, R. et al. CD209L/L-SIGN and CD209/DC-SIGN act as receptors for SARS-CoV-2. Preprint at *bioRxiv* https://doi.org/10.1101/2020.06.22.165803 (2020).
14. Soh, W. T. et al. The N-terminal domain of spike glycoprotein mediates SARS-CoV-2 infection by associating with L-SIGN and DC-SIGN. Preprint at *bioRxiv* https://doi.org/10.1101/2020.11.05.369264 (2020).
15. Wang, K. et al. CD147-spike protein is a novel route for SARS-CoV-2 infection to host cells. *Signal Transduct. Target. Ther.* **5**, 283 (2020).
16. Cantuti-Castelvetri, L. et al. Neuropilin-1 facilitates SARS-CoV-2 cell entry and infectivity. *Science* **370**, 856–860 (2020).
17. Clausen, T. M. et al. SARS-CoV-2 infection depends on cellular heparan sulfate and ACE2. *Cell* **183**, 1043–1057 (2020).
18. Thépaut, M. et al. DC/L-SIGN recognition of spike glycoprotein promotes SARS-CoV-2 trans-infection and can be inhibited by a glycomimetic antagonist. *PLoS Pathog.* **17**, e1009576 (2021).
19. Izquierdo-Useros, N. et al. Siglec-1 is a novel dendritic cell receptor that mediates HIV-1 *trans*-infection through recognition of viral membrane gangliosides. *PLoS Biol.* **10**, e1001448 (2012).
20. Travaglini, K. J. et al. A molecular cell atlas of the human lung from single-cell RNA sequencing. *Nature* **587**, 619–625 (2020).
21. Ren, X. et al. COVID-19 immune features revealed by a large-scale single cell transcriptome atlas. *Cell* **184**, 1895–1913.e19 (2021).
22. Liao, M. et al. Single-cell landscape of bronchoalveolar immune cells in patients with COVID-19. *Nat. Med.* **26**, 842–844 (2020).
23. Perez-Zsolt, D. et al. Siglec-1 on dendritic cells mediates SARS-CoV-2 *trans*-infection of target cells while on macrophages triggers proinflammatory responses. Preprint at *bioRxiv* https://doi.org/10.1101/2021.05.11.443572 (2021).
24. Lu, Q. et al. SARS-CoV-2 exacerbates proinflammatory responses in myeloid cells through C-type lectin receptors and Tweety family member 2. *Immunity* **54**, 1304–1319.e9 (2021).
25. Pinto, D. et al. Cross-neutralization of SARS-CoV-2 by a human monoclonal SARS-CoV antibody. *Nature* **583**, 290–295 (2020).
26. McCallum, M. et al. N-terminal domain antigenic mapping reveals a site of vulnerability for SARS-CoV-2. *Cell* **184**, 2332–2347.e16 (2021).
27. Chan, J. F. et al. Simulation of the clinical and pathological manifestations of coronavirus disease 2019 (COVID-19) in a golden Syrian hamster model: implications for disease pathogenesis and transmissibility. *Clin. Infect. Dis.* **71**, 2428–2446 (2020).
28. Baum, A. et al. REGN-COV2 antibodies prevent and treat SARS-CoV-2 infection in rhesus macaques and hamsters. *Science* **370**, 1110–1115 (2020).
29. Gupta, A. et al. Early Covid-19 treatment with SARS-CoV-2 neutralizing antibody sotrovimab. Preprint at *medRxiv* https://doi.org/10.1101/2021.05.27.21257096 (2021).
30. Buchrieser, J. et al. Syncytia formation by SARS-CoV-2-infected cells. *EMBO J.* **40**, e107405 (2021).
31. Bussani, R. et al. Persistence of viral RNA, pneumocyte syncytia and thrombosis are hallmarks of advanced COVID-19 pathology. *EBioMed.* **61**, 103104 (2020).
32. Walls, A. C. et al. Unexpected receptor functional mimicry elucidates activation of coronavirus fusion. *Cell* **176**, 1026–1039.e15 (2019).
33. Pinto, D. et al. Broad betacoronavirus neutralization by a stem helix-specific human antibody. *Science* **373**, 1109–1116 (2021).
34. Starr, T. N. et al. SARS-CoV-2 RBD antibodies that maximize breadth and resistance to escape. *Nature* **597**, 97–102 (2021).
35. Wan, Y. et al. Molecular mechanism for antibody-dependent enhancement of coronavirus entry. *J. Virol.* **94**, 69–15 (2020).
36. Blanco-Melo, D. et al. Imbalanced host response to SARS-CoV-2 drives development of COVID-19. *Cell* **181**, 1036–1045.e9 (2020).
37. Ziegler, C. G. K. et al. SARS-CoV-2 receptor ACE2 is an interferon-stimulated gene in human airway epithelial cells and is detected in specific cell subsets across tissues. *Cell* **181**, 1016–1035.e19 (2020).
38. Chang, Y. C. & Nizet, V. Siglecs at the host–pathogen interface. *Adv. Exp. Med. Biol.* **1204**, 197–214 (2020).
39. Cathcart, A. L. et al. The dual function monoclonal antibodies VIR-7831 and VIR-7832 demonstrate potent in vitro and in vivo activity against SARS-CoV-2. Preprint at *bioRxiv* https://doi.org/10.1101/2021.03.09.434607 (2021).
40. Sewald, X. et al. Retroviruses use CD169-mediated trans-infection of permissive lymphocytes to establish infection. *Science* **350**, 563–567 (2015).
41. Uchil, P. D. et al. A protective role for the lectin CD169/Siglec-1 against a pathogenic murine retrovirus. *Cell Host Microbe* **25**, 87–100.e10 (2019).
42. Asarnow, D. et al. Structural insight into SARS-CoV-2 neutralizing antibodies and modulation of syncytia. *Cell* **184**, 3192–3204.e16 (2021).
43. Xu, Z. et al. Pathological findings of COVID-19 associated with acute respiratory distress syndrome. *Lancet Respir. Med.* **8**, 420–422 (2020).
44. Tian, S. et al. Pulmonary pathology of early-phase 2019 novel coronavirus (COVID-19) pneumonia in two patients with lung cancer. *J. Thorac. Oncol.* **15**, 700–704 (2020).

Methods

Ethics statement

The institutional review board on biomedical research of the Hospital Germans Trias i Pujol (HUGTiP) approved this study. The biologic biosafety committee of the Research Institute Germans Trias i Pujol approved the execution of SARS-CoV-2 experiments at the BSL3 laboratory of the Center of Bioimaging and comparative imaging (CMCIB).

Generation of stable overexpression cell lines

Lentiviruses were generated by co-transfection of Lenti-X 293T cells (Takara) with lentiviral expression plasmids encoding DC-SIGN (CD209), L-SIGN (CLEC4M), SIGLEC1, TMPRSS2 or ACE2 (all obtained from Genecopoeia) and the respective lentiviral helper plasmids. Forty-eight hours after transfection, lentivirus in the supernatant was collected and concentrated by ultracentrifugation for 2 h at 20,000 rpm. Lenti-X 293T (Takara), Vero E6 (ATCC), MRC5 (Sigma-Aldrich), A549 (ATCC) or HeLa (ATCC) cells were transduced in the presence of 6 μg ml^{-1} polybrene (Millipore) for 24 h. Cell lines overexpressing two transgenes were transduced subsequently. Selection with puromycin and/or blasticidin (Gibco) was started two days after transduction and selection reagent was kept in the growth medium for all subsequent culturing. Single-cell clones were derived from the A549-ACE2-TMPRSS2 cell line, all other cell lines represent cell pools.

SARS-CoV-2 neutralization

Cells cultured in DMEM supplemented with 10% FBS (VWR) and 1× Penicillin/Streptomycin (Thermo Fisher Scientific) were seeded in black 96-well plates at 20,000 cells per well. Serial 1:4 dilutions of the monoclonal antibodies were incubated with 200 pfu of SARS-CoV-2 (isolate USA-WA1/2020, passage 3, passaged in Vero E6 cells) for 30 min at 37 °C in a BSL-3 facility. Cell supernatant was removed and the virus–antibody mixture was added to the cells. Twenty-four hours after infection, cells were fixed with 4% paraformaldehyde for 30 min, followed by two PBS (pH 7.4) washes and permeabilization with 0.25% Triton X-100 in PBS for 30 min. After blocking in 5% milk powder/PBS for 30 min, cells were incubated with a primary antibody targeting SARS-CoV-2 nucleocapsid protein (Sino Biological, catalogue (cat.) no. 40143-R001) at a 1:2,000 dilution for 1 h. After washing and incubation with a secondary Alexa Fluor 647-labelled antibody mixed with 1 μg ml^{-1} Hoechst33342 for 1 h, plates were imaged on an automated cell-imaging reader (Cytation 5, Biotek) and nucleocapsid-positive cells were counted using the manufacturer's supplied software (Gen5 v3.08).

SARS-CoV-2-Nluc neutralization

Neutralization was determined using SARS-CoV-2-Nluc, an infectious clone of SARS-CoV-2 (based on strain 2019-nCoV/USA_WA1/2020) encoding nanoluciferase in place of the viral ORF7, which demonstrates comparable growth kinetics to wild type virus[45]. Cells were seeded into black-walled, clear-bottom 96-well plates at 20,000 cells per well (293T cells were seeded into poly-L-lysine-coated wells at 35,000 cells per well) and cultured overnight at 37 °C. The next day, 9-point fourfold serial dilutions of antibodies were prepared in infection medium (DMEM + 10% FBS). SARS-CoV-2-Nluc was diluted in infection medium at the indicated multiplicity of infection (MOI), added to the antibody dilutions and incubated for 30 min at 37 °C. Medium was removed from the cells, monoclonal antibody–virus complexes were added, and cells were incubated at 37 °C for 24 h. Medium was removed from the cells, Nano-Glo luciferase substrate (Promega) was added according to the manufacturer's recommendations, incubated for 10 min at room temperature and luciferase signal was quantified on a VICTOR Nivo plate reader using Nivo v3.0.2 software (Perkin Elmer).

SARS-CoV-2 pseudotyped VSV production and neutralization

To generate SARS-CoV-2 pseudotyped VSV, Lenti-X 293T cells (Takara) were seeded in 10-cm dishes for 80% next day confluency. The next day, cells were transfected with a plasmid encoding for SARS-CoV-2 S-glycoprotein (YP_009724390.1) harbouring a C-terminal 19-amino acid truncation using TransIT-Lenti (Mirus Bio) according to the manufacturer's instructions. One day after transfection, cells were infected with VSV(G*ΔG-luciferase) (Kerafast) at an MOI of 3 infectious units per cell. Viral inoculum was washed off after 1 h and cells were incubated for another day at 37 °C. The cell supernatant containing SARS-CoV-2 pseudotyped VSV was collected at day 2 after transfection, centrifuged at 1,000*g* for 5 min to remove cellular debris, aliquoted and frozen at −80 °C.

For viral neutralization, cells were seeded into black-walled, clear-bottom 96-well plates at 20,000 cells per well (293T cells were seeded into poly-L-lysine-coated wells at 35,000 cells per well) and cultured overnight at 37 °C. The next day, 9-point fourfold serial dilutions of antibodies were prepared in medium. SARS-CoV-2 pseudotyped VSV was diluted 1:30 in media in the presence of 100 ng ml^{-1} anti-VSV-G antibody (clone 8G5F11, Absolute Antibody) and added 1:1 to each antibody dilution. Virus:antibody mixtures were incubated for 1 h at 37 °C. Media was removed from the cells and 50 μl of virus:antibody mixtures were added to the cells. One hour post-infection, 100 μl of medium was added to all wells and incubated for 17–20 h at 37 °C. Medium was removed and 50 μl of Bio-Glo reagent (Promega) was added to each well. The plate was shaken on a plate shaker at 300 rpm at room temperature for 15 min and RLUs were read on an EnSight plate reader using Kaleido v3.0 software (Perkin-Elmer).

Transfection-based attachment receptor screen

Lenti-X 293T cells (Takara) were transfected with plasmids encoding the following receptor candidates (all purchased from Genecopoeia): ACE2 (NM_021804), DC-SIGN (NM_021155), L-SIGN (BC110614), LGALS3 (NM_002306), SIGLEC1 (NM_023068), SIGLEC3 (XM_057602), SIGLEC9 (BC035365), SIGLEC10 (NM_033130), MGL (NM_182906), MINCLE (NM_014358), CD147 (NM_198589), ASGR1 (NM_001671.4), ASGR2 (NM_080913), NRP1 (NM_003873). One day after transfection, cells were infected with SARS-CoV-2 pseudotyped VSV at 1:20 dilution in the presence of 100 ng ml^{-1} anti-VSV-G antibody (clone 8G5F11, Absolute Antibody) at 37 °C. One hour after infection, 100 μl of medium was added to all wells and incubated for 17–20 h at 37 °C. Medium was removed and 50 μl of Bio-Glo reagent (Promega) was added to each well. The plate was shaken on a plate shaker at 300 rpm at room temperature for 15 min and readings in RLU were taken on an EnSight plate reader (Perkin-Elmer).

siRNA-mediated knockdown of ACE2

For reverse transfection of 293T or HuH7 cells, siRNA pools specific for ACE2 (Dharmacon ON-TARGETplus SMARTpool, L-005755-00-0005, pool of 4 individual siRNAs with target sequences: GACAAGAGCAAACG GUUGA, GCGAGUGGCUAAUUUGAAA, GCCAUUAUAUGAAGAGUAU, GGACAAGUUUAACCACGAA) or non-targeting control pool (Dharmacon ON-TARGETplus Non-targeting Pool, D-001810-10-05) were preincubated at 20 nM with Lipofectamine RNAiMAX (Thermo Fisher Scientific) in black-walled clear-bottom 96-well plates according to the manufacturer's instructions. Fifteen-thousand 293T cells or 10,000 HuH7 cells were seeded on top and incubated at 37 °C. After four days, cells were infected with SARS-CoV-2 pseudotyped VSV as described above.

Trans infection using Hela cells

Parental HeLa cells or HeLa cells stably expressing DC-SIGN, L-SIGN or SIGLEC1 were seeded at 5,000 cells per well in black-walled clear-bottom 96-well plates. One day later, cells reached about 50% confluency and were inoculated with SARS-CoV-2 pseudotyped VSV at 1:10 dilution in the presence of 100 ng/mL anti-VSV-G antibody (clone 8G5F11, Absolute Antibody) at 37 °C for 2 h. For antibody-mediated inhibition of *trans* infection, cells were pre-incubated with 10 μg ml^{-1} anti-SIGLEC1 antibody (Biolegend, clone 7-239) for 30 min. After 2 h inoculation, cells were washed 4 times with complete medium and

10,000 VeroE6-TMPRSS2 cells per well were added and incubated for 17–20 h at 37 °C for *trans* infection. Medium was removed and 50 µl of Bio-Glo reagent (Promega) was added to each well. The plate was shaken on a plate shaker at 300 rpm at room temperature for 15 min and RLUs were read on an EnSight plate reader using Kaleido v3.0 software (Perkin-Elmer).

Cell–cell fusion of CHO-S cells

CHO cells stably expressing SARS-CoV-2 S-glycoprotein were seeded in 96-well plates for microscopy (Thermo Fisher Scientific) at 12,500 cells per well and the following day, different concentrations of monoclonal antibodies and nuclei marker Hoechst (final dilution 1:1,000) were added to the cells and incubated for additional 24 h. Fusion degree was established using the Cytation 5 Imager (BioTek) and an object detection protocol was used to detect nuclei as objects and measure their size. The nuclei of fused cells (that is, syncytia) are found aggregated at the centre of the syncytia and are recognized as a unique large object that is gated according to its size. The area of the objects in fused cells divided by the total area of all the object multiplied by 100 provides the percentage of fused cells

Negative-stain electron microscopy imaging the fusogenic rearrangement of soluble S trimers

SARS-CoV-2 S ectodomain trimer was engineered as follow and recombinantly expressed. The SARS-CoV-2 S(D614G) has a mu-phosphatase signal peptide beginning at Q14, a mutated S1/S2 cleavage site (SGAR), ends at residue K1211 and is followed by a TEV cleavage, fold-on trimerization motif, and an 8× His tag in the pCMV vector. Ten micromolar S was incubated with 13 µM Fab protein for 1 or 48 h at room temperature. Samples were diluted to 0.01 mg ml^{-1} immediately before protein was adsorbed to glow-discharged carbon-coated copper grids for ~30 s before 2% uranyl formate staining. Micrographs were recorded using the Leginon software[46] on a 100kV FEI Tecnai G2 Spirit with a Gatan Ultrascan 4000 4k × 4k CCD camera at 67,000 nominal magnification. The defocus ranged from 1.0 to 2.0 µm and the pixel size was 1.6 Å.

Cryo-electron microscopy

SARS-CoV-2 HexaPro S[47] at 1.2 mg ml^{-1} was incubated with 1.2 fold molar excess of recombinantly purified S2X58 for 10 s at room temperature before application onto a freshly glow discharged 2.0/2.0 UltrAuFoil grid (200 mesh). Plunge freezing used a vitrobot MarkIV (Thermo Fisher Scientific) using a blot force of 0 and 6.5 s blot time at 100% humidity and 23 °C.

Data were acquired using an FEI Titan Krios transmission electron microscope operated at 300 kV and equipped with a Gatan K2 Summit direct detector and Gatan Quantum GIF energy filter, operated in zero-loss mode with a slit width of 20 eV. Automated data collection was carried out using Leginon[46] at a nominal magnification of 130,000× with a pixel size of 0.525 Å and stage tilt angles up to 35°. The dose rate was adjusted to 8 counts per pixel s^{-1}, and each movie was acquired in super-resolution mode fractionated in 50 frames of 200 ms. 4,126 micrographs were collected with a defocus range between −0.5 and −3.0 µm. Movie frame alignment, estimation of the microscope contrast-transfer function parameters, particle picking, and extraction were carried out using Warp[48]. Particle images were extracted with a box size of 800 binned to 400 pixels^2, yielding a pixel size of 1.05 Å.

Two rounds of reference-free 2D classification were performed using CryoSPARC[49] to select well-defined particle images. These selected particles were subjected to two rounds of 3D classification with 50 iterations each (angular sampling 7.5° for 25 iterations and 1.8° with local search for 25 iterations), using our previously reported closed SARS-CoV-2 S structure as initial model (PDB 6VXX) in Relion[50]. 3D refinements were carried out using non-uniform refinement along with per-particle defocus refinement in CryoSPARC[51]. Selected particle images were subjected to the Bayesian polishing procedure implemented in Relion3.0[52] before performing another round of non-uniform refinement in CryoSPARC followed by per-particle defocus refinement and again non-uniform refinement. Local resolution estimation, filtering, and sharpening were carried out using CryoSPARC. Reported resolutions are based on the gold-standard Fourier shell correlation (FSC) of 0.143 criterion and Fourier shell correlation curves were corrected for the effects of soft masking by high-resolution noise substitution. UCSF ChimeraX[53] and Coot[54] were used to fit atomic models into the cryo-EM maps.

Immunofluorescence analysis

HEK 293T-derived cell lines were seeded onto poly-D-lysine-coated 96-well plates (Sigma-Aldrich) and fixed 24 h after seeding with 4% paraformaldehyde for 30 min, followed by 2 PBS (pH 7.4) washes and permeabilization with 0.25% Triton X-100 in PBS for 30 min. Cells were incubated with primary antibodies anti-DC-SIGN/L-SIGN (Biolegend, cat. no. 845002, 1:500 dilution), anti-DC-SIGN (Cell Signaling, cat. no. 13193S, 1:500 dilution), anti-SIGLEC1 (Biolegend, cat. no. 346002, 1:500 dilution) or anti-ACE2 (R&D Systems, cat. no. AF933, 1:200 dilution) diluted in 3% milk powder/PBS for 2 h at room temperature. After washing and incubation with a secondary Alexa Fluor 647-labeled antibody mixed with 1 µg ml^{-1} Hoechst33342 for 1 h, plates were imaged on an inverted fluorescence microscope (Echo Revolve).

ACE2 and *TMPRSS2* RT–qPCR

RNA was extracted from the cells using the NucleoSpin RNA Plus kit (Macherey-Nagel) according to the manufacturer's protocol. Human airway epithelial (HAE) cells were provided by MatTek Life Sciences (MatTek EpiAirway). RNA was reverse transcribed using the High Capacity cDNA Reverse Transcription kit (Applied Biosystems) according to the manufacturer's instructions. Intracellular levels of *ACE2* (forward primer: CAAGAGCAAACGGTTGAACAC, reverse primer: CCAGAGC CTCTCATTGTAGTCT), *HPRT* (forward primer: CCTGGCGTCGTGATT AGTG, reverse primer: ACACCCTTTCCAAATCCTCAG) and *TMPRSS2* (forward primer: CAAGTGCTCCRACTCTGGGAT, reverse primer: AACACACCGRTTCTCGTCCTC) were quantified using the Luna Universal qPCR Master Mix (New England Biolabs) according to the manufacturer's protocol. Levels of *ACE2* and *TMPRSS2* were normalized to *HPRT*. Hela cells were used as the reference sample. All quantitative PCRs were run on a QuantStudio 3 Real-Time PCR System (Applied Biosystems).

SARS-CoV-2 S(D614G) production and biotinylation

Prefusion-stabilized SARS-CoV-2 S(D614G) (comprising amino acids Q14 to K1211) with a C-terminal TEV cleavage site, T4 bacteriophage fibritin foldon, 8× His, Avi and EPEA tags was transfected into HEK 293 Freestyle cells, using 293 fectin as a transfection reagent. Cells were left to produce protein for 3 days at 37 °C. Afterwards, supernatant was collected by centrifuging cells for 30 min at 500*g*, followed by another spin for 30 min at 4,000*g*. Cell culture supernatant was filtered through a 0.2-µm filter and loaded onto a 5-ml C-tag affinity matrix column, pre-equilibrated with 50 mM Tris pH 8 and 200 mM NaCl. SARS-CoV-2 D614G S was eluted, using 10 column volumes of 100 mM Tris, 200 mM NaCl and 3.8 mM SEPEA peptide. Elution peak was concentrated and injected on a Superose 6 increase 10/300 GL gel filtration column, using 50 mM Tris pH 8 and 200 mM NaCl as a running buffer. Size-exclusion fractions corresponding to monodisperse SARS-CoV-2 S(D614G) were collected and flash frozen in liquid nitrogen for storage at −80 °C. Purified SARS-CoV-2 S(D614G) protein was biotinylated using BirA500 biotinylation kit from Avidity. To 50 µg of S protein, 5 µg of BirA, and 11 µl of BiomixA and BiomixB was added. Final S protein concentration during the biotinylation reaction was ~1 µM. The reaction was left to proceed for 16 h at 4 °C. Then, protein was desalted using two Zeba spin columns pre-equilibrated with 1× PBS pH 7.4.

Flow cytometry analysis for DC-SIGN, L-SIGN, SIGLEC1 and ACE-2

HEK 293T cells expressing DC-SIGN, L-SIGN, SIGLEC1 or ACE2 were resuspended at 4 × 10^6 cells per ml and 100 µl per well were seeded onto

V-bottom 96-well plates (Corning, 3894). The plate was centrifuged at 2,000 rpm for 5 min and washed with PBS (pH 7.4). The cells were resuspended in 200 µl of PBS containing Ghost violet 510 viability dye (Cell Signaling, cat. no. 13-0870-T100, 1:1,000 dilution), incubated for 15 min on ice and then washed. The cells were resuspended in 100 µl of fluorescence-activated cell sorting (FACS) buffer prepared with 0.5% BSA (Sigma-Aldrich) in PBS containing the primary antibodies at a 1:100 dilution: mouse anti-DC/L-SIGN (Biolegend, cat. no. 845002), rabbit anti-DC-SIGN (Cell Signaling, cat. no. 13193), mouse anti-SIGLEC1 (Biolegend, cat. no. 346002) or goat anti-ACE2 (R&D Systems, cat. no. AF933). After 1 h incubation on ice, the cells were washed two times and resuspended in FACS buffer containing the Alexa Fluor 488-labelled secondary antibodies at a 1:200 dilution: goat anti-mouse (Invitrogen cat. no. A11001), goat anti-rabbit (Invitrogen cat. no. A11008) or donkey anti-goat (Invitrogen cat. no. A11055). After incubation for 45 min on ice, the cells were washed 3 times with 200µl of FACS buffer and fixed with 200 µl of 4% PFA (Alfa Aesar) for 15 min at room temperature. Cells were washed 3 times, resuspended in 200 µl of FACS buffer and analysed by flow cytometry using the CytoFLEX flow cytometer (Beckman Coulter).

Flow cytometry of SARS-CoV-2 S and RBD binding to cells

Biotinylated SARS-CoV-2 S(D614G) protein ($Spike_{biotin}$, generated in-house) or the biotinylated SARS-CoV-2 S receptor-binding domain (RBD_{biotin}, Sino Biological, 40592-V08B) were incubated with Alexa Fluor 647 streptavidin (AF647-strep, Invitrogen, S21374) at a 1:20 ratio by volume for 20 min at room temperature. The labelled proteins were then stored at 4 °C until further use. Cells were dissociated with TrypLE Express (Gibco, 12605-010) and 10^5 cells were transferred to each well of a 96-well V bottom plate (Corning, 3894). Cells were washed twice in flow cytometry buffer (2% FBS in PBS (without Ca and Mg)) and stained with $Spike_{biotin}$-AF647-strep at a final concentration of 20 µg ml^{-1} or RBD_{biotin}-AF647-strep at a final concentration of 7.5 µg ml^{-1} for 1 h on ice. Stained cells were washed twice with flow cytometry buffer, resuspended in 1% PFA (Electron Microscopy Sciences, 15714-S) and analysed with the Cytoflex LX (Beckman Coulter).

Recombinant expression of SARS-CoV-2-specific monoclonal antibodies

Human monoclonal antibodies were isolated from plasma cells or memory B cells of SARS-CoV-2-immune donors, as previously described[25,55,56]. Recombinant antibodies were expressed in ExpiCHO cells at 37 °C and 8% CO_2. Cells were transfected using ExpiFectamine. Transfected cells were supplemented one day after transfection with ExpiCHO Feed and ExpiFectamine CHO Enhancer. Cell culture supernatant was collected 8 days after transfection and filtered through a 0.2-µm filter. Recombinant antibodies were affinity purified on an ÄKTAxpress FPLC device using 5 ml HiTrap MabSelect PrismA columns followed by buffer exchange to Histidine buffer (20 mM histidine, 8% sucrose, pH 6) using HiPrep 26/10 desalting columns.

SARS-CoV-2 *trans*-infection assay on primary cells

Cell lines used have been described[57]. Isolation and culture of primary cells was performed as described[58]. In brief, peripheral blood mononuclear cells were obtained with a Ficoll–Hypaque gradient (Alere Technologies) from blood donors and monocyte populations (>90% CD14$^+$) were isolated with CD14 negative selection magnetic beads (Miltenyi Biotec). Macrophages were obtained by culturing these cells in the presence of 100 ng ml^{-1} of macrophage colony-stimulating factor (M-CSF) for 7 days and replacing media and cytokines every 2 days. DCs were obtained culturing these cells in the presence of both 1,000 IU ml^{-1} granulocyte-macrophage colony-stimulating factor (GM-CSF) and interleukin-4 (R&D Systems) for 7 days and replacing medium and cytokines every 2 days. Activated cells were differentiated by culturing myeloid cells at day 5 for 2 more days in the presence of 1,000 IU ml^{-1} of interferon-α (IFNα) (Sigma-Aldrich) or 100 ng ml^{-1} LPS (Sigma-Aldrich). The SARS-CoV-2 viral strain used on primary cells was isolated in March 2020 from a nasopharyngeal swab as described[57]. The virus was propagated for two passages and a virus stock was prepared by collecting the supernatant from Vero E6 cells. The genomic sequence was deposited at the GISAID repository (http://gisaid.org) with accession ID EPI_ISL_510689. For *trans* infection, cells were pre-incubated for 15 min at room temperature with 10 µg ml^{-1} anti-SIGLEC1 7–239 (Abcam) or IgG1 isotype control (BD Biosciences), or left untreated before viral exposure. Uptake experiments with SARS-CoV-2 were performed by pulsing 0.1×10^6 DCs with 200 µl SARS-CoV-2 with $10^{6.15}$ median tissue culture infectious dose ($TCID_{50}$) per ml for 3 h at 37 °C. After extensive washing, cells were co-cultured at a ratio 3:1 with HEK 293T cells expressing or not expressing ACE2 and TMPRSS-2. Six days later, the amount of viral release to the supernatant was measured with a SARS-CoV-2 nucleocapsid protein High-sensitivity Quantitative ELISA (Immuno Diagnostics).

SIGLEC1 surface expression analysis by FACS

A total of 2.5×10^5 myeloid cells was blocked with 1 mg ml^{-1} of human IgGs and stained with anti-SIGLEC1–PE or matched isotype–PE control (BioLegend) at 4 °C for 30 min. The mean number of SIGLEC1 monoclonal antibody binding sites per cell was obtained with a Quantibrite kit (Becton Dickinson), subtracting values obtained for isotype control. Samples were analysed with a Canto Flow Cytometer using Flow Jo software to evaluate collected data.

SARS-CoV-2 infection model in hamster

Virus preparation. The SARS-CoV-2 strain used in this study, BetaCov/Belgium/GHB-03021/2020 (EPI ISL 109 407976|2020-02-03), was recovered from a nasopharyngeal swab taken from an asymptomatic patient infected with SARS-CoV-2—confirmed by quantitative PCR with reverse transcription (RT–qPCR)—who returned from Wuhan, China in February 2020. A close relation with the prototypic Wuhan-Hu-1 2019-nCoV (GenBank accession 112 number MN908947.3) strain was confirmed by phylogenetic analysis. Infectious virus was isolated by serial passaging on HuH7 and Vero E6 cells;[59] passage 6 virus was used for the study described here. The titre of the virus stock was determined by end-point dilution on Vero E6 cells by the Reed and Muench method[60]. Live virus-related work was conducted in the high-containment ABSL3 and BSL3+ facilities of the KU Leuven Rega Institute (3CAPS) under licenses AMV 30112018 SBB 219 2018 0892 and AMV 23102017 SBB 219 20170589 according to institutional guidelines.

Cells. Vero E6 cells (African green monkey kidney, ATCC CRL-1586) were cultured in minimal essential medium (Gibco) supplemented with 10% fetal bovine serum (Integro), 1% L- glutamine (Gibco) and 1% bicarbonate (Gibco). End-point titrations were performed with medium containing 2% fetal bovine serum instead of 10%.

SARS-CoV-2 infection model in hamsters. The hamster infection model of SARS-CoV-2 has been described[59,61]. The specific study design is shown in the schematic below. In brief, wild-type Syrian Golden hamsters (*Mesocricetus auratus*) were purchased from Janvier Laboratories and were housed per two in ventilated isolator cages (IsoCage N Biocontainment System, Tecniplast) with ad libitum access to food and water and cage enrichment (wood block). The animals were acclimatized for four days before the start of the study. Housing conditions and experimental procedures were approved by the ethics committee of animal experimentation of KU Leuven (license P065- 2020). Sample size was dimensioned in order to have a significant difference of at least 1 log viral RNA (effect size $d = 2.004$) between control and treated groups, by using a two-tailed t-test with 80% power and an α error of 0.05, calculated with G*Power 3.1 software. Female 6- to 8-week-old hamsters were anaesthetized with ketamine/xylazine/atropine and inoculated intranasally with 50 µl containing 2×10^6 $TCID_{50}$ SARS-CoV-2 (day 0).

Treatment regimen. Hamsters were allocated into different monoclonal antibody or dosing groups at random. Animals were prophylactically treated 48 h before infection by intraperitoneal administration and monitored for appearance, behaviour and weight. At day 4 after infection, hamsters were euthanized by intraperitoneal injection of 500 µl Dolethal (200 mg ml^{-1} sodium pentobarbital) (Vétoquinol). Lungs were collected and viral RNA and infectious virus were quantified by RT–qPCR and end-point virus titration, respectively. Blood samples were collected before infection for PK analysis. The circulating antibody levels were measured by mesoscale bridging ELISA using an anti-human LS mutation monoclonal antibody for capture and anti-human CH2 monoclonal antibody for detection[34].

SARS-CoV-2 RT–qPCR. Collected lung tissues were homogenized using bead disruption (Precellys) in 350µl RLT buffer (RNeasyMinikit,Qiagen) and centrifuged (10,000 rpm, 5 min) to pellet the cell debris. RNA was extracted according to the manufacturer's instructions. Of 50 µl eluate, 4 µl was used as a template in RT–qPCR reactions. RT–qPCR was performed on a LightCycler96 platform (Roche) using the iTaq Universal Probes One-Step RT-qPCR kit (BioRad) with N2 primers and probes targeting the nucleocapsid[59]. Standards of SARS-CoV-2 cDNA (IDT) were used to express viral genome copies per mg tissue or per ml serum.

End-point virus titrations. Lung tissues were homogenized using bead disruption (Precellys) in 350 µL minimal essential medium and centrifuged (10,000 rpm, 5 min, 4 °C) to pellet the cell debris. To quantify infectious SARS-CoV-2 particles, end-point titrations were performed on confluent Vero E6 cells in 96-well plates. Viral titres were calculated by the Reed and Muench method[60] using the Lindenbach calculator and were expressed as $TCID_{50}$ per mg tissue. The samples for RNA and virus titration were run by the technicians in a blinded manner, without knowing the treatment group.

Histology. For histological examination, lungs were fixed overnight in 4% formaldehyde and embedded in paraffin. Tissue sections (5 µm) were analysed after staining with haematoxylin and eosin and scored blindly for lung damage by an expert pathologist. The scored parameters, to which a cumulative score of 1 to 3 was attributed, were the following: congestion, intra-alveolar haemorrhagic, apoptotic bodies in bronchus wall, necrotizing bronchiolitis, perivascular oedema, bronchopneumonia, perivascular inflammation, peribronchial inflammation and vasculitis.

Binding of immunocomplexes to hamster monocytes. Immunocomplexes were generated by complexing S309 monoclonal antibody (hamster IgG, either wt or N297A) with a biotinylated anti-idiotype Fab fragment and Alexa Fluor 488-streptavidin, using a precise molar ratio (4:8:1, respectively). Pre-generated fluorescent immunocomplexes were serially diluted and incubated at 4 °C for 3 h with freshly revitalized hamster splenocytes, obtained from a naive animal. Cellular binding was then evaluated by cytometry upon exclusion of dead cells and physical gating on monocyte population. Results are expressed as Alexa Fluor 488 mean florescent intensity of the entire monocyte population.

Binding of immunocomplexes to hamster FcgRIV and human FcgRIIIA by biolayer interferometry. Antibody immunocomplexes were first generated by cross-linking hamster S309 and S309-N297A with a specific F(ab)2 anti-S309 idiotype monoclonal antibodies (2:1 µg ml^{-1} ratio) for 40 min at room temperature. Recombinant golden hamster (GH) FcγRIV and biotinylated human FcγRIIIA (Acro Biosystems) were diluted to 0.25 and 0.5 µg ml^{-1} respectively in kinetic buffer (PBS + BSA 0.01%, pH 7.1) and immobilized on anti-His-Penta or streptavidin SAX Biosensors (FortéBio) for 10 min. FcγRs-coated biosensors were incubated for 5 min with immunocomplexes mixture (4.5 µg ml^{-1}), to allow association, followed by a 5-min dissociation step. The shift in the biolayer interferometry signal generated by change in molecular binding was recorded in real time using an Octet RED96 system (FortéBio). Binding raw data were exported and plotted using GraphPad Prism software (V9).

Bioinformatic analyses. Processed Human Lung Cell Atlas (HLCA) data and cell-type annotations[20] were downloaded from Github (https://github.com/krasnowlab/HLCA). Processed single-cell transcriptome data and annotation of lung epithelial and immune cells from individuals infected with SARS-CoV-2[21,22] were downloaded from the NCBI GEO database (ID: GSE158055) and Github (https://github.com/zhangzlab/covid_balf). Available sequence data from the second single-cell transcriptomics study by Liao et al. [22] were downloaded from NCBI SRA (ID: PRJNA608742) for inspection of reads corresponding to viral RNA using NCBI MagicBlast and SAMtools. Reads that supported a junction between the 5′ leader sequence and the transcription regulatory sequence (TRS) preceding open reading frames for viral genes were counted as evidence of subgenomic mRNA, a surrogate readout for viral replication. Such reads constituted a small fraction of TRS-containing viral reads, ranging from undetectable to 3.4%. The proportion of single guide RNA relative to genomic RNA was estimated by counting TRS-containing reads supporting a leader–TRS junction. Criteria and methods for detection of leader-TRS junction reads were adapted from Alexandersen et al. [62]. The viral genome reference and TRS annotation were based on Wuhan-Hu-1 NC_045512.2/MN908947[63]. Only two samples from individuals with severe COVID-19 had detectable leader–TRS junction reads (SRR11181958 and SRR11181959). Summary visualizations and analyses for the datasets above were performed using R and the following R packages: data.table, ggplot2, cowplot, scales, RColorBrewer, viridis, scater, and SingleCellExperiment.

Statistics and reproducibility

If not stated otherwise, all experiments were performed with at least three biological replicates for each condition. Experiments were independently repeated at least two times, and one representative dataset is shown. All error bars throughout the study represent the s.d. Statistical tests are detailed in the respective figure legends.

Reporting summary

Further information on research design is available in the Nature Research Reporting Summary linked to this paper.

Data availability

FACS gating strategies are provided as Supplementary Information. The cryo-EM maps have been deposited to the Electron Microscopy Data Bank with accession numbers EMD-24607 (two RBDs open) and EMD-24608 (three RBDs open). Single-cell transcriptome datasets used in this study had been published previously: NCBI Gene Expression Omnibus (ID: GSE158055), NCBI Sequence Read Archive (ID: PRJNA608742). All further relevant source data that support the findings of this study are available from the corresponding author upon reasonable request. Source data are provided with this paper.

45. Xie, X. et al. A nanoluciferase SARS-CoV-2 for rapid neutralization testing and screening of anti-infective drugs for COVID-19. *Nat. Commun.* **11**, 5214 (2020).
46. Suloway, C. et al. Automated molecular microscopy: the new Leginon system. *J. Struct. Biol.* **151**, 41–60 (2005).
47. Hsieh, C. L. et al. Structure-based design of prefusion-stabilized SARS-CoV-2 spikes. *Science* **369**, 1501–1505 (2020).
48. Tegunov, D. & Cramer, P. Real-time cryo-electron microscopy data preprocessing with Warp. *Nat. Methods* **16**, 1146–1152 (2019).
49. Punjani, A., Rubinstein, J. L., Fleet, D. J. & Brubaker, M. A. cryoSPARC: algorithms for rapid unsupervised cryo-EM structure determination. *Nat. Methods* **14**, 290–296 (2017).
50. Zivanov, J. et al. New tools for automated high-resolution cryo-EM structure determination in RELION-3. *Elife* **7**, e42166 (2018).
51. Punjani, A., Zhang, H. & Fleet, D. J. Non-uniform refinement: adaptive regularization improves single-particle cryo-EM reconstruction. *Nat. Methods* **17**, 1214–1221 (2020).

52. Zivanov, J., Nakane, T. & Scheres, S. H. W. A Bayesian approach to beam-induced motion correction in cryo-EM single-particle analysis. *IUCrJ* **6**, 5–17 (2019).
53. Pettersen, E. F. et al. UCSF ChimeraX: structure visualization for researchers, educators, and developers. *Protein Sci.* **30**, 70–82 (2021).
54. Casanal, A., Lohkamp, B. & Emsley, P. Current developments in Coot for macromolecular model building of electron cryo-microscopy and crystallographic data. *Protein Sci.* **29**, 1069–1078 (2020).
55. Corti, D. et al. A neutralizing antibody selected from plasma cells that binds to group 1 and group 2 influenza A hemagglutinins. *Science* **333**, 850–856 (2011).
56. Tortorici, M. A. et al. Ultrapotent human antibodies protect against SARS-CoV-2 challenge via multiple mechanisms. *Science* **370**, 950–957 (2020).
57. Rodon, J. et al. Identification of plitidepsin as potent inhibitor of SARS-CoV-2-induced cytopathic effect after a drug repurposing screen. *Front. Pharmacol.* **12**, 646676 (2021).
58. Perez-Zsolt, D. et al. Anti-Siglec-1 antibodies block Ebola viral uptake and decrease cytoplasmic viral entry. *Nat. Microbiol.* **4**, 1558–1570 (2019).
59. Boudewijns, R. et al. STAT2 signaling restricts viral dissemination but drives severe pneumonia in SARS-CoV-2 infected hamsters. *Nat. Commun.* **11**, 5838 (2020).
60. Reed, L. J. & Muench, H. A simple method of estimating fifty per cent endpoints. *Am. J. Epidemiol.* **27**, 493–497 (1938).
61. Sanchez-Felipe, L. et al. A single-dose live-attenuated YF17D-vectored SARS-CoV-2 vaccine candidate. *Nature* **590**, 320–325 (2021).
62. Alexandersen, S., Chamings, A. & Bhatta, T. R. SARS-CoV-2 genomic and subgenomic RNAs in diagnostic samples are not an indicator of active replication. *Nat. Commun.* **11**, 6059 (2020).
63. Wu, F. et al. A new coronavirus associated with human respiratory disease in China. *Nature* **579**, 265–269 (2020).
64. Chua, R. L. et al. COVID-19 severity correlates with airway epithelium–immune cell interactions identified by single-cell analysis. *Nat. Biotechnol.* **38**, 970–979 (2020).
65. Bost, P. et al. Host–viral infection maps reveal signatures of severe COVID-19 patients. *Cell* **181**, 1475–1488.e12 (2020).
66. Tortorici, M. A. et al. Broad sarbecovirus neutralization by a human monoclonal antibody. *Nature* **597**, 103–108 (2021).
67. Shi, R. et al. A human neutralizing antibody targets the receptor-binding site of SARS-CoV-2. *Nature* **584**, 120–124 (2020).
68. Jones, B. E. et al. The neutralizing antibody, LY-CoV555, protects against SARS-CoV-2 infection in nonhuman primates. *Sci. Transl. Med.* **13**, abf1906 (2021).
69. ACTIV-3/TICO LY-CoV555 Study Group A neutralizing monoclonal antibody for hospitalized patients with Covid-19. *N. Engl. J. Med.* **384**, 905–914 (2021).
70. Kim, C. et al. A therapeutic neutralizing antibody targeting receptor binding domain of SARS-CoV-2 spike protein. *Nat. Commun.* **12**, 288 (2021).

Acknowledgements We thank D.R.-R., J.M.-B., D.P.-Z., I.E. and X.M.-T. from IrsiCaixa for their contribution to *trans*-infection experiments. J.V.-A. and N.I.-U. are part of the CBIG consortium (constituted by IRTA-CReSA, BSC and IrsiCaixa) and are supported by Grifols. N.I.-U. is supported by grant PID2020-117145RB-I00 from the Spanish Ministry of Science and Innovation. J.M.-P. is supported by grant PID2019-109870RB-I00 from the Spanish Ministry of Science and Innovation and in part by Grifols. The authors acknowledge the crowdfunding initiative #Yomecorono (https://www.yomecorono.com). This study was supported by the National Institute of Allergy and Infectious Diseases (DP1AI158186 and HHSN272201700059C to D.V.), a Pew Biomedical Scholars Award (D.V.), Investigators in the Pathogenesis of Infectious Disease Awards from the Burroughs Wellcome Fund (D.V.) and Fast Grants (D.V.). The funders had no role in study design, data collection and analysis, decision to publish, or preparation of the manuscript. The following reagent was deposited by the Centers for Disease Control and Prevention and obtained through BEI Resources, NIAID, NIH: SARS-Related Coronavirus 2, Isolate USA-WA1/2020, NR-52281.

Author contributions Conceived the study: F.A.L., L.S., A.L., L.P., D.V., A.T. and D.C. Designed the study and experiments: F.A.L., L.S., M.M.-R., J.N., F.B. and D.C. Performed in vitro virological experiments: F.A.L., F.B., Y.-J.P., S.B., M.M.-R., J.N., A.C.W., J.E.B., J.Z., H.K. and M.A. Electron microscopy data collection and analysis: Y.-J.P., A.C.W. and J.E.B. Produced antibodies for in vitro and in vivo studies: S.J. and E.C. Primary cell analyses: J.V.-A., J.M.-P. and N.I.-U. Recombinant glycoproteins production: J.E.B., M.M., A.J. and E.D. Hamster model and data analysis: F.B. Bioinformatic analysis: L.S. and A.T. Manuscript writing: F.A.L, F.B., L.P., D.V., A.L., A.T. and D.C. Supervision: L.P., D.V., H.W.V., A.T. and D.C.

Competing interests F.A.L., L.S., F.B., S.B., M.M.-R., J.N., J.Z., H.K., M.A., M.M., E.D., S.J., E.C., H.W.V., A.L., L.P., A.T. and D.C. are employees of Vir Biotechnology and may hold shares in Vir Biotechnology. H.W.V. is a founder of PierianDx and Casma Therapeutics. L.P. is a former employee and shareholder in Regeneron Pharmaceuticals. Neither company provided funding for this work or is performing related work. D.V. is a consultant for Vir Biotechnology. The laboratory of D.V. has received a sponsored research agreement from Vir Biotechnology. A patent application related to SIGLEC1 and SARS-CoV-2 recognition has been filed by IrsiCaixa (US 63/152,346). J.M.-P. reports institutional grants and educational and consultancy fees from AbiVax, Astra-Zeneca, Gilead Sciences, Grifols, Janssen, Merck and ViiV Healthcare. N.I.-U. reports institutional grants from Pharma Mar, Dentaid and Palobiofarma. The remaining authors declare no competing interests.

Additional information
Supplementary information The online version contains supplementary material available at https://doi.org/10.1038/s41586-021-03925-1.

Correspondence and requests for materials should be addressed to Amalio Telenti or Davide Corti.

Peer review information *Nature* thanks Stanley Perlman and the other, anonymous, reviewer(s) for their contribution to the peer review of this work.

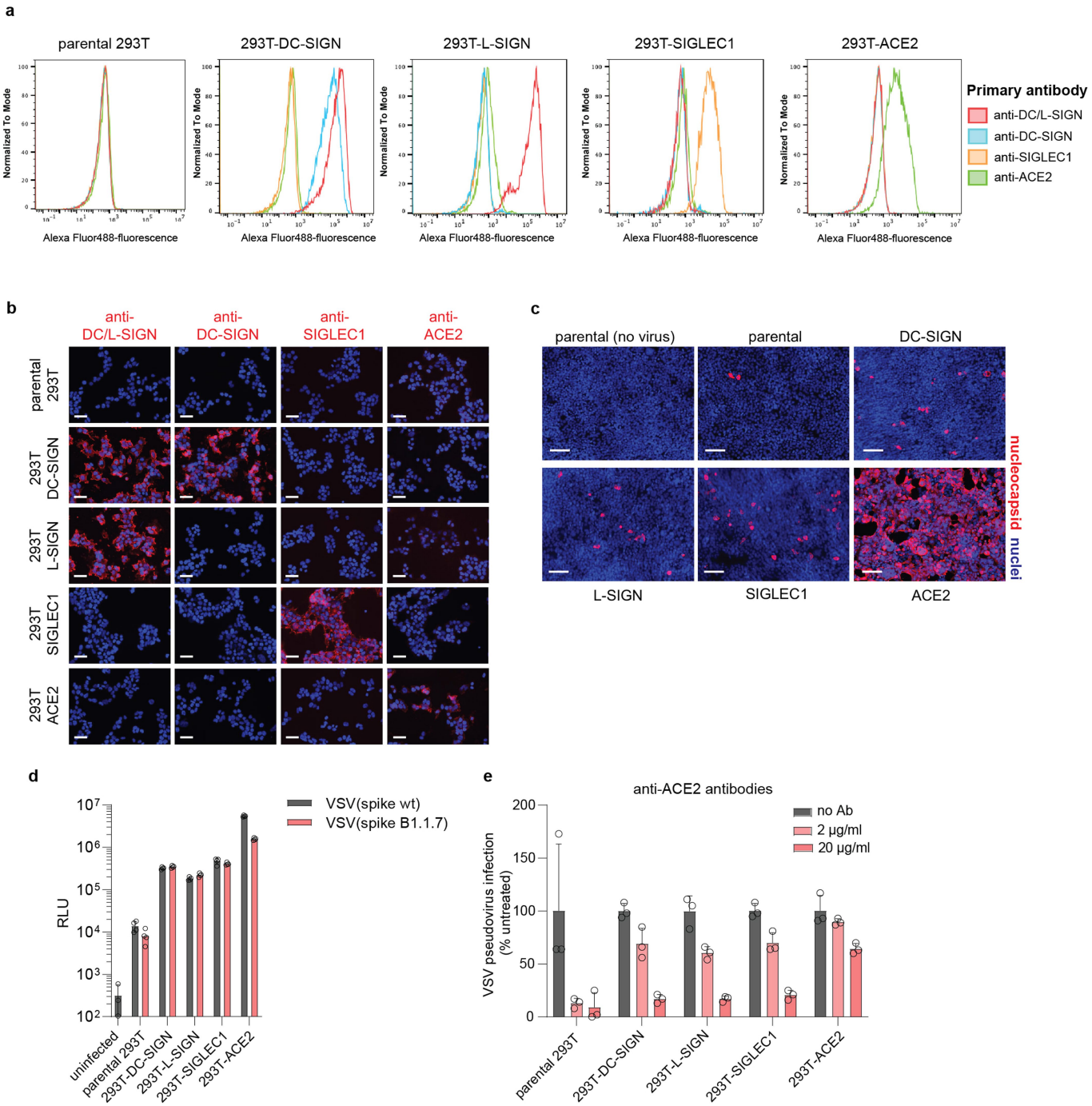

Extended Data Fig. 1 | Characterization of DC-SIGN, L-SIGN and SIGLEC-1 as SARS-CoV-2 attachment factors. a–b, Binding of antibodies targeting DC/-L-SIGN, DC-SIGN, SIGLEC1 or ACE2 on HEK293T stably over-expressing the respective attachment receptors was analyzed by flow cytometry (a) and immunofluorescence analysis (b) (scale bar: 50 µm). **c**, Stable HEK293T cell lines overexpressing lectins or ACE2 were infected with authentic SARS-CoV-2 (MOI 0.1) and immunostained at 24 h for nucleocapsid protein (red) (scale bar: 100 µm). **d**, HEK293T cells over-expressing the respective attachment receptors were infected with VSV-SARS-COV-2 wildtype spike (grey bars) or spike bearing mutations of the B.1.1.7 variant (red bars). Luminescence was analyzed one day post infection ($n = 4$ biologically independent replicates). **e**, Stable cell lines were incubated with anti-ACE2 polyclonal antibodies and infected with VSV-SARS-CoV-2 ($n = 3$ biologically independent replicates).

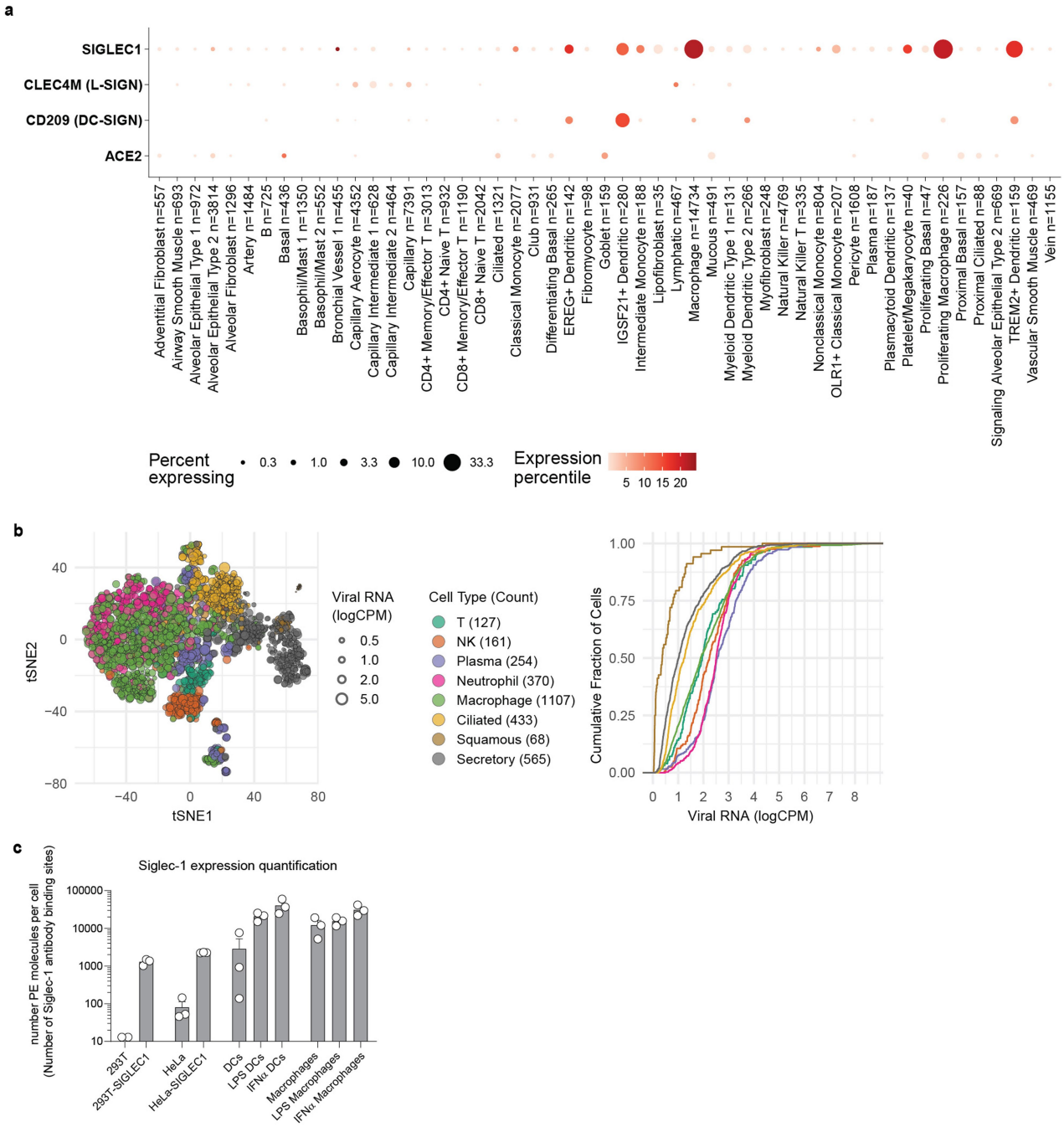

Extended Data Fig. 2 | Expression of attachment receptors in infected tissues. a, Distribution and expression of ACE2, DC-SIGN, L-SIGN, and SIGLEC1 in the human lung cell atlas. **b**, Major cell types with detectable SARS-CoV-2 genome in bronchoalveolar lavage fluid and sputum of severe COVID-19 patients. Left panel shows a t-SNE embedding of single-cell gene expression profiles coloured by cell type and sized by viral load (logCPM); right panel, distribution plots by annotated cell type denote the cumulative fraction of cells (y-axis) with detected viral RNA per cell up to the corresponding logCPM value (x-axis). Viral RNA is also found in neutrophils, plasma and T cells – an observation that has been reported previously[21,64–70] **c**, SIGLEC1 surface expression comparison. Mean number of SIGLEC1 antibody binding sites per cell displayed by SIGLEC1 stably transduced cell lines and different myeloid cells left untreated or exposed to IFNα or LPS for 48 h and assessed by quantitative FACS analysis. Data show mean values and SEM from one experiment including cells from 3 donors.

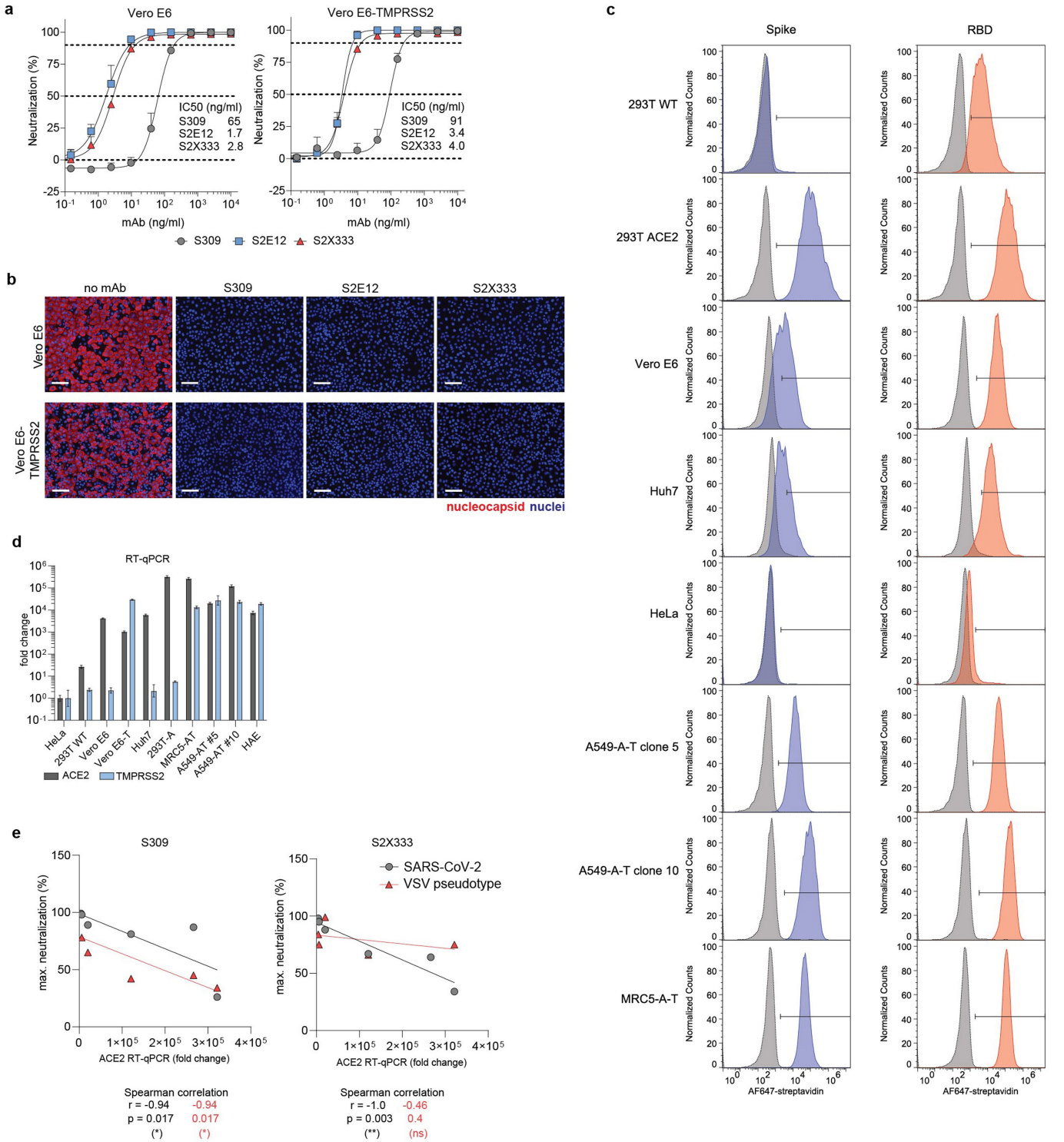

Extended Data Fig. 3 | Characterization of SARS-CoV-2-susceptible cell lines. a, SARS-CoV-2 neutralization with S309, S2E12 and S2X333 on Vero E6 or Vero E6-TMPRSS2 cells. Cells were infected with SARS-CoV-2 (isolate USA-WA1/2020) at MOI 0.01 in the presence of the respective mAbs. Cells were fixed 24h post infection, viral nucleocapsid protein was immunostained and quantified ($n = 3$ biologically independent replicates). **b**, IFA images of experiment in (a): SARS-CoV-2 neutralization with 10 µg/ml of S309, S2E12 and S2X333 on Vero E6 or Vero E6-TMPRSS2 cells (scale bar: 100 µm). **c**, Purified, fluorescently-labelled SARS-CoV-2 spike protein or RBD protein was incubated with the indicated cell lines and protein binding was quantified by flow cytometry. **d**, Cellular ACE2 and TMPRSS2 transcripts were quantified by RT-qPCR. Expression levels were adjusted by HPRT levels and are presented as normalized to HeLa cell levels, showing the mean of technical triplicates. **e**, Correlation analysis between ACE2 transcript levels and maximum antibody neutralization in all SARS-CoV-2-susceptible cell lines. Nonparametric, two-tailed Spearman correlation was calculated using GraphPad Prism.

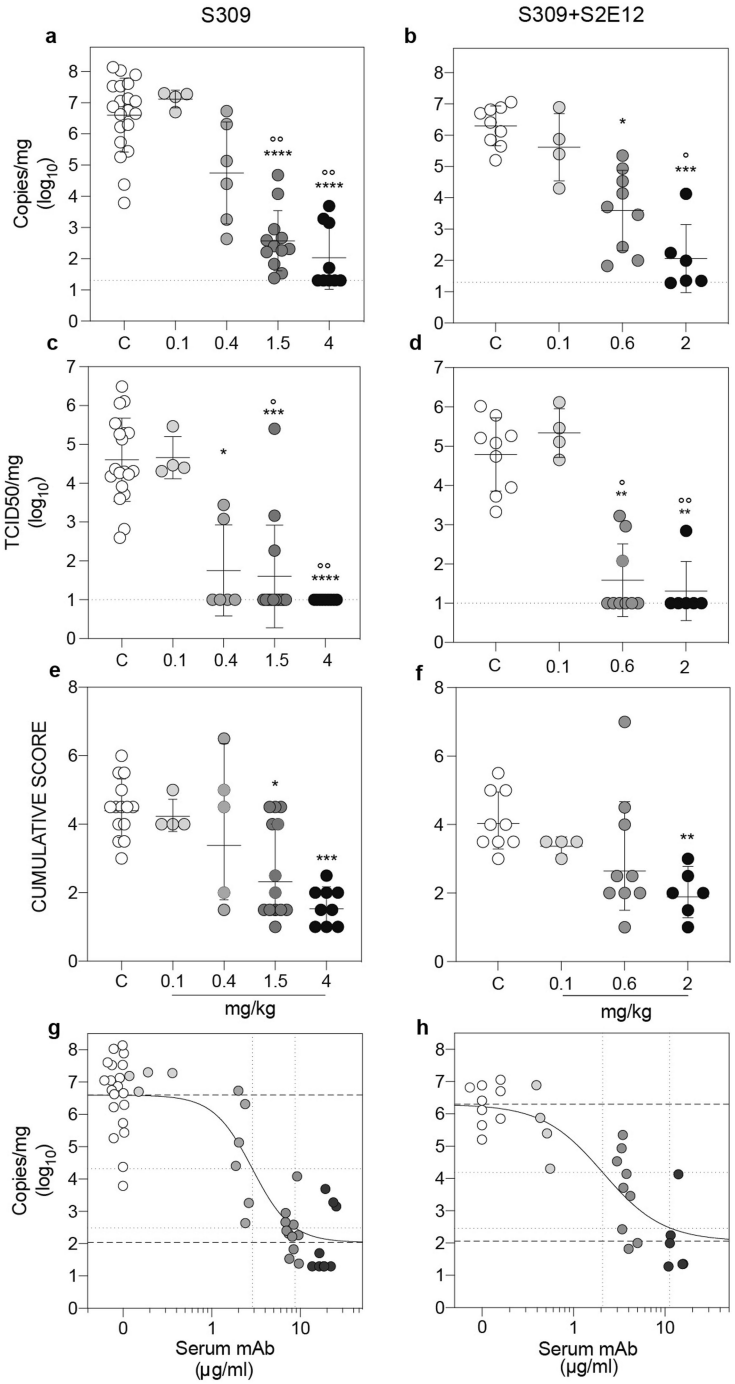

Extended Data Fig. 4 | S309 or a cocktail of S309 and S2E12 provide robust in vivo protection against SARS-CoV-2 challenge. Syrian hamsters (n = 4–19) were injected with the indicated amount of mAb(s) 48 h before intra-nasal challenge with SARS-CoV-2. **a**–**b**, Quantification of viral RNA in the lungs 4 days post-infection. **** p < 0.0001 vs C; °° p = 0.0023 4 vs 0.1, p = 0,0096 1.5 vs 0.1. **c**–**d**, Quantification of replicating virus in lung homogenates harvested 4 days post infection using a TCID50 assay. **** p < 0.0001 vs C; *** p = 0.0002 1.5 vs C; * p = 0.0146 0.4 vs C; °° p = 0.0056 4 vs 0.1; ° p = 0.0236 1.5 vs 0.1. **e**–**f**, Histopathological score of the lung tissue was assessed 4 days post infection. *** p = 0.0005 vs C; * p = 0.0369 vs C. Nonparametric one-way ANOVA, Kruskal-Wallis test with Dunn's multiple comparisons test (alpha threshold 0.05). Data are from at least 2 independent experiments, except the group dosed with 0.1 mg/kg (n = 4) that was tested once. **g**–**h**, Efficacy plots based on the correlation between the level of serum antibody measured at the time of infection and the level of SARS-CoV2 (viral RNA) measured in lungs on day 4 after infection. The dotted lines represents EC50 and EC90 for viral reduction (EC90 of S309 alone vs S309 + S2E12: 9 vs 11 µg/ml, respectively).

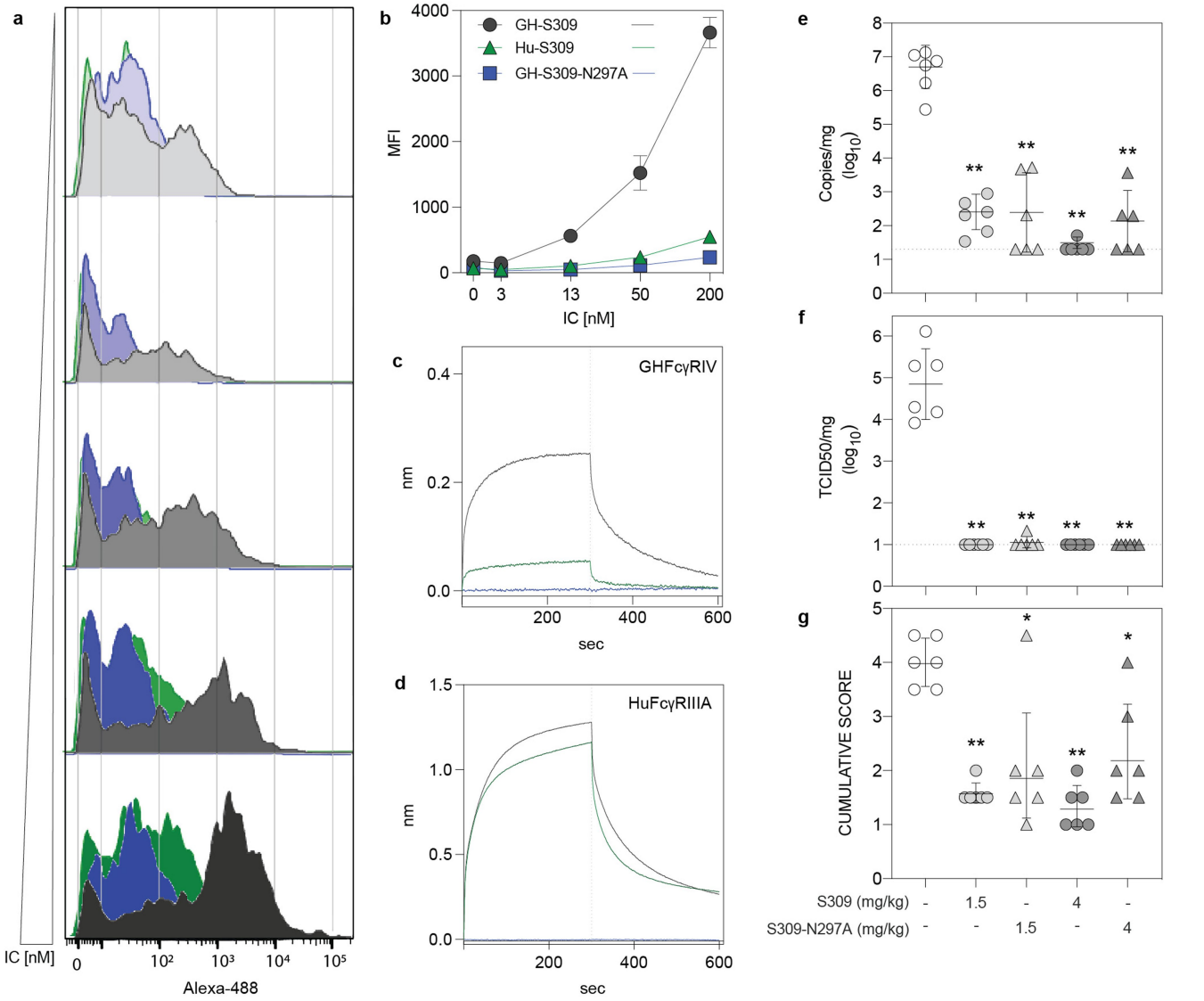

Extended Data Fig. 5 | Binding of immunocomplexes to hamster splenocytes/FcgR and role of host effector function in SARS-CoV-2 challenge. Alexa-488 fluorescent IC were titrated (0–200 nM range) and incubated with total naïve hamster splenocytes. Binding was revealed with a cytometer upon exclusion of dead/apoptotic cells and physical gating on bona fide monocyte population. **a**, fluorescent intensity associated to hamster cells of immune-complex (IC) made with either hamster (GH-S309, dark grey and GH-S309-N297A, blue) or human (Hu-S309, green) Fc antibodies. A single replicate of two is shown. **b**, relative Alexa-488 mean fluorescent intensity of the replicates measured on the entire monocyte population. Data are from a single representative experiment repeated three times with similar results. **c**–**d**, kinetics of binding of the same hamster and human ICs to hamster FcgRIV (panel C) and human FcgRIIIA (panel D) by Octet BLI analysis. **e**–**g**, Syrian hamsters ($n = 6$) were injected with the indicated amount (mg/kg) of hamster IgG2a S309 either wt or Fc silenced (S309-N297A). **e**, Quantification of viral RNA in the lung 4 days post infection. ** p = 0.0022 vs control. **f**, Quantification of replicating virus in the lung 4 days post infection. ** p = 0.0022 vs control **g**, Histopathological score in the lung 4 days post infection. ** p = 0.0022 vs C; * p = 0.04111.5 (N297A) vs C, p = 0.0130 4 (N297A) vs control. Control animals (white symbols) were injected with 4 mg/kg unrelated control isotype mAb. 2-tailed nonparametric Mann-Whitney t test (alpha threshold 0.05). Data are from a single experiment.

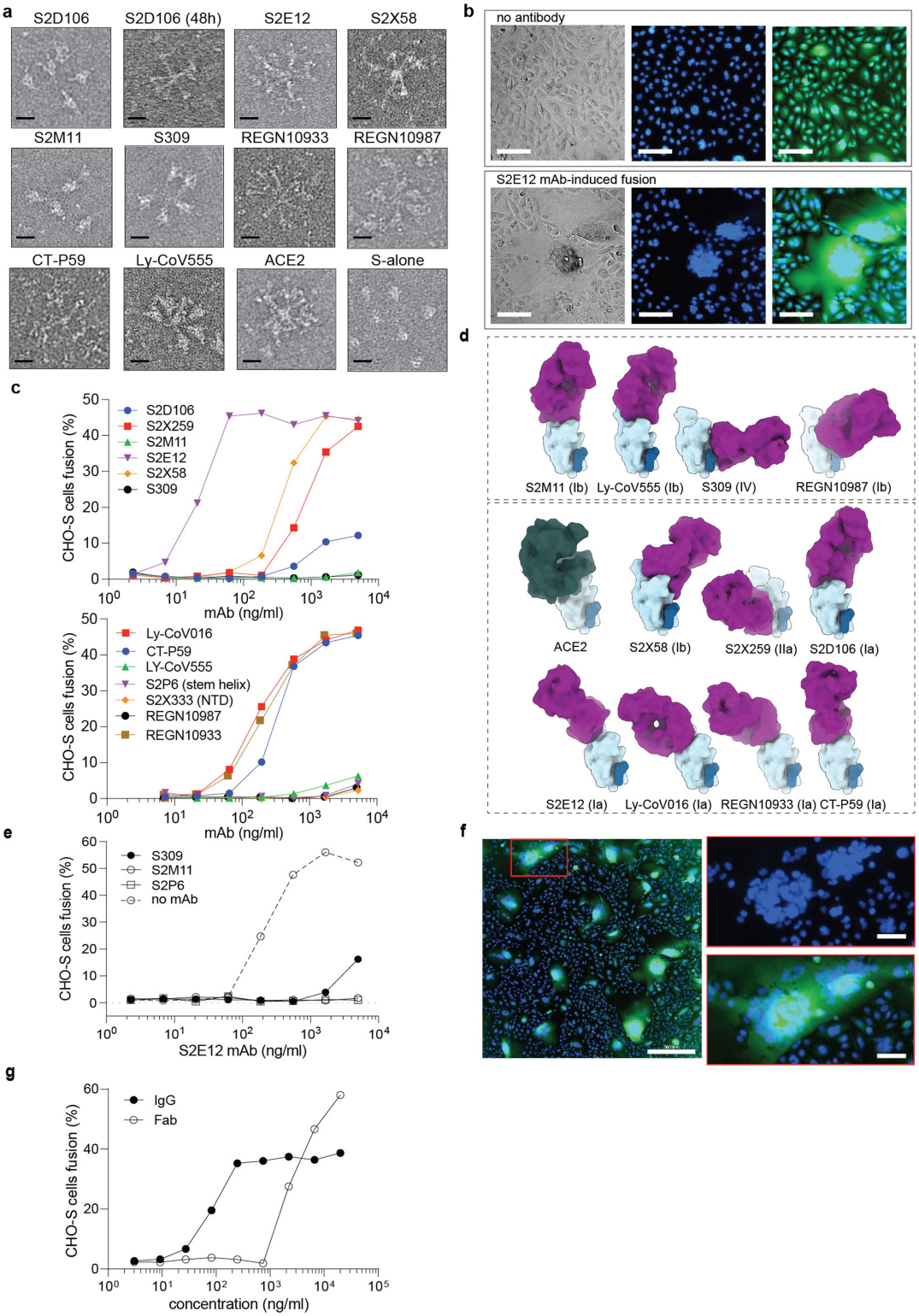

Extended Data Fig. 6 | RBM mAbs trigger the fusogenic rearrangement of the S protein and promote membrane fusion. a, MAbs or soluble ACE2 were incubated for 1 h with native-like soluble prefusion S trimer of SARS-CoV-2 to track by negative stain EM imaging the fusogenic rearrangement of soluble S trimers visible as rosettes (scale bar: 20 nm). 100 micrographs per sample were analyzed. **b**, Cell-cell fusion of CHO cells expressing SARS-CoV-2 S (CHO-S) on the plasma membrane in the absence (upper panel) or presence of 5 µg/ml of S2E12 mAb (lower panel) as detected by immunofluorescence. Nuclei stained with Hoechst dye; cytoplasm stained with CellTracker Green (scale bar: 100 µm). **c**, CHO-S cell-cell fusion mediated by different spike-specific mAbs quantified as described in Methods. **d**, Structures of 11 Fab-RBD complexes related to mAbs used in (c) (RBD orientation is fixed) and of ACE2-RBD as determined by a combination of X-ray crystallography and cryo-EM analysis (PDBs, Extended Data Table 1). Shown in parentheses the RBD antigenic site as defined according to Piccoli et al. [5]. **e**, Inhibition of S2E12-induced cell-cell fusion performed as in (c) by a fixed amount (15 µg/ml) of indicated mAbs. **f**, Trans-fusion of S-positive CHO cells with S-negative fluorescently-labelled CHO cells. Staining as in (b) (scale bar: 300 µm, inlet 50 µm). **g**, CHO-S cells were seeded in 96-well plates an incubated with S2E12 IgG or Fab. Cell-Cell fusion was quantified by imaging as described in methods.

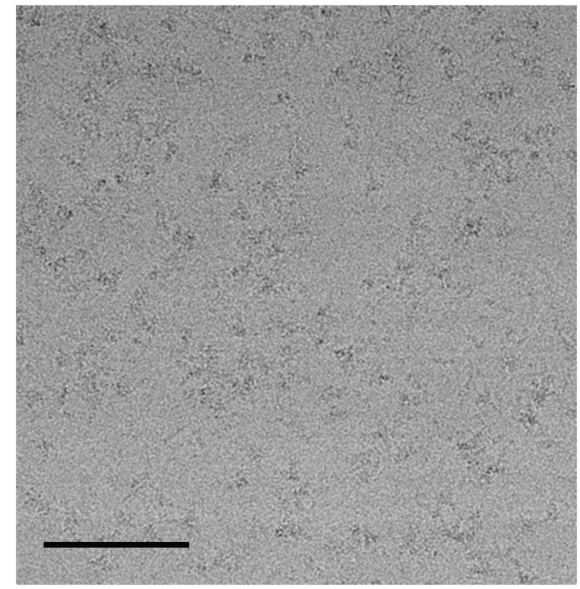

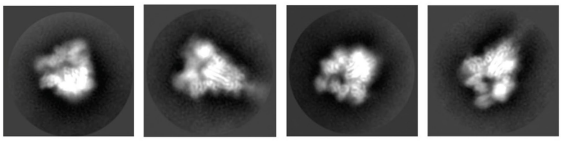

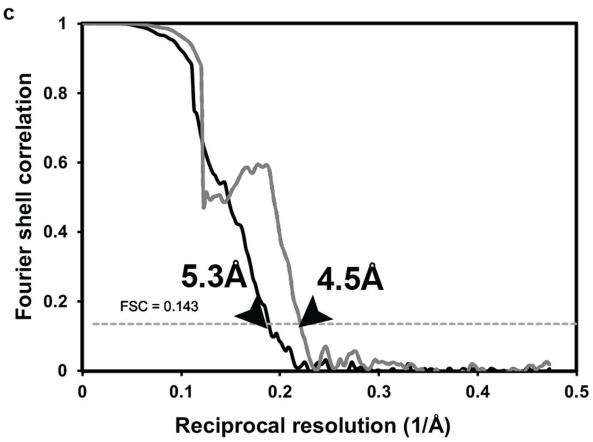

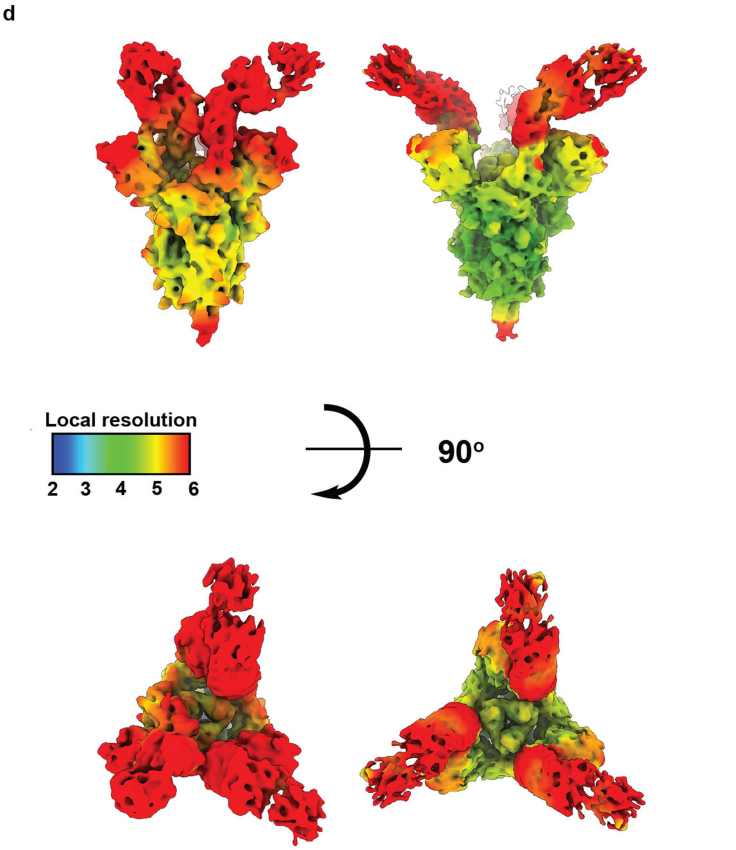

e

	SARS-CoV-2 S/S2X58 (Three RBDs open) EMD-24608	SARS-CoV-2 S/S2X58 (One RBD closed) EMD-24607
Data collection and processing		
Magnification	130,000	130,000
Voltage (kV)	300	300
Electron exposure (e–/Å^2)	70	70
Defocus range (μm)	-0.5 – -3.0	-0.5 – -3.0
Pixel size (Å)	0.525	0.525
Symmetry imposed	C3	C1
Initial particle images (no.)	62,205	68,783
Map resolution (Å)	4.5	5.3
FSC threshold	0.143	0.143
Map sharpening *B* factor (Å^2)	-147	-241

Extended Data Fig. 7 | Data collection and processing of the S/S2X58 complex cryoEM datasets. a-b, Representative electron micrograph and 2D class averages of SARS-CoV-2 S in complex with the S2X58 Fab embedded in vitreous ice. Scale bar: 400 Å. **c**, Gold-standard Fourier shell correlation curves for the S2X58-bound SARS-CoV-2 S trimer in one RBD closed (black line) and three RBDs open conformations (gray line). The 0.143 cutoff is indicated by a horizontal dashed line. Due to steric clashes between the S2X58 Fab and the NTD of a neighboring monomer in the closed S state, this mAb appears to conformationally select the open RBDs, thus explaining its fusogenic activity. **d**, Local resolution maps calculated using cryoSPARC for the SARS-CoV-2 S/S2X58 Fab complex structure with one RBD closed and three RBDs open shown in two orthogonal orientations. **e**, Cryo-EM data collection statistics.

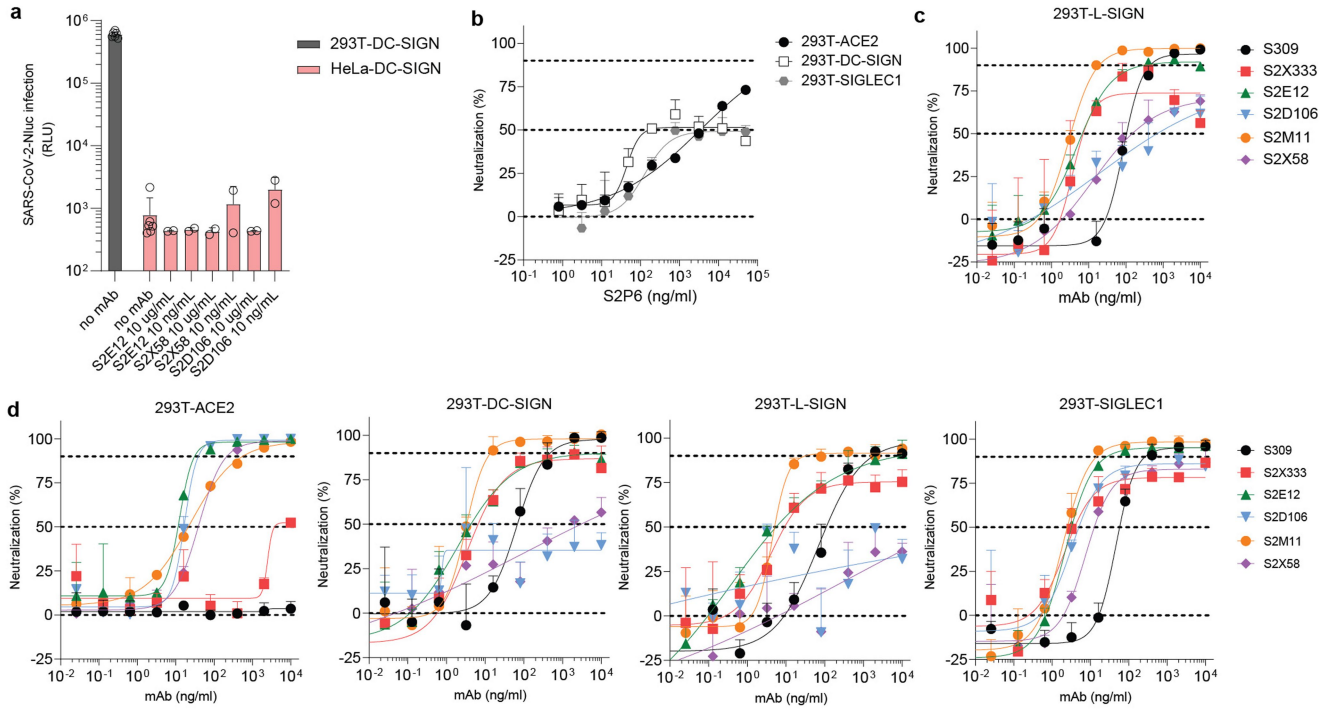

e

	Classes of antibodies					
Mechanism	RBM (Ia-IIa)	RBM (Ib)	S2M11 Ib-lock	NTD	S309 (IV)	Stem helix
Fusogenic S rearrangement	++/+	-(+æ)	-	-	-	-
ACE2 blockade	+	+	+	-	-	-
Fusion inhibition*	+	ND	+	ND	+	+
Effector functions**	-	+	+	++	++	++
Neut. on ACE2^{hi} cells	+	+	+	-	-	-
Neut.on ACE2^{lo} cells	+	+	+	+	+	+
Neut. on lectin enh. infection	+/-	ND	+	+	+	+/-

Extended Data Fig. 8 | SARS-CoV-2 live virus neutralization. a, HeLa cells expressing DC-SIGN are refractory to SARS-CoV-2 infection. HEK293T or HeLa cells stably expressing DC-SIGN were infected with SARS-CoV-2-Nluc at MOI 0.04 in the presence of the indicated antibodies. Infection was analyzed by quantification of luminescent signal at 24 h post infection (n=2 biologically independent replicates). **b**, Neutralization of infection by SARS-CoV-2-Nluc pre-incubated with the stem helix antibody S2P6 on HEK293T cell lines stably overexpressing lectins or ACE2. Infection was measured by luciferase signal 24h post infection (n = 3 biologically independent replicates) **c**, Infection neutralization by authentic SARS-CoV-2-Nluc pre-incubated with indicated mAbs on HEK293T cell lines stably overexpressing L-SIGN (n=3 biologically independent replicates). Infection was measured by luciferase signal 24h post infection (n = 3 biologically independent replicates). **d**, HEK293T cells stably expressing ACE2 or lectins were infected with SARS-CoV-2 at MOI 0.02 in the presence of the indicated mAbs. Cells were fixed 24h post infection, viral nucleocapsid protein was immunostained and positive cells were quantified (n = 3 biologically independent replicates). **e**, Summary of the mechanisms of action of different classes of spike-specific mAbs based on this and previous studies. *, mAb-mediated inhibition of fusion between CHO-spike cells and ACE2^{+} Vero-E6 cells; **, based on mAb-dependent activation of human FcgRs performed with a bioluminescent reporter assay as in ref. [25æ], S2X58 binds to open RBD due to a conformational clash with neighboring NTD.

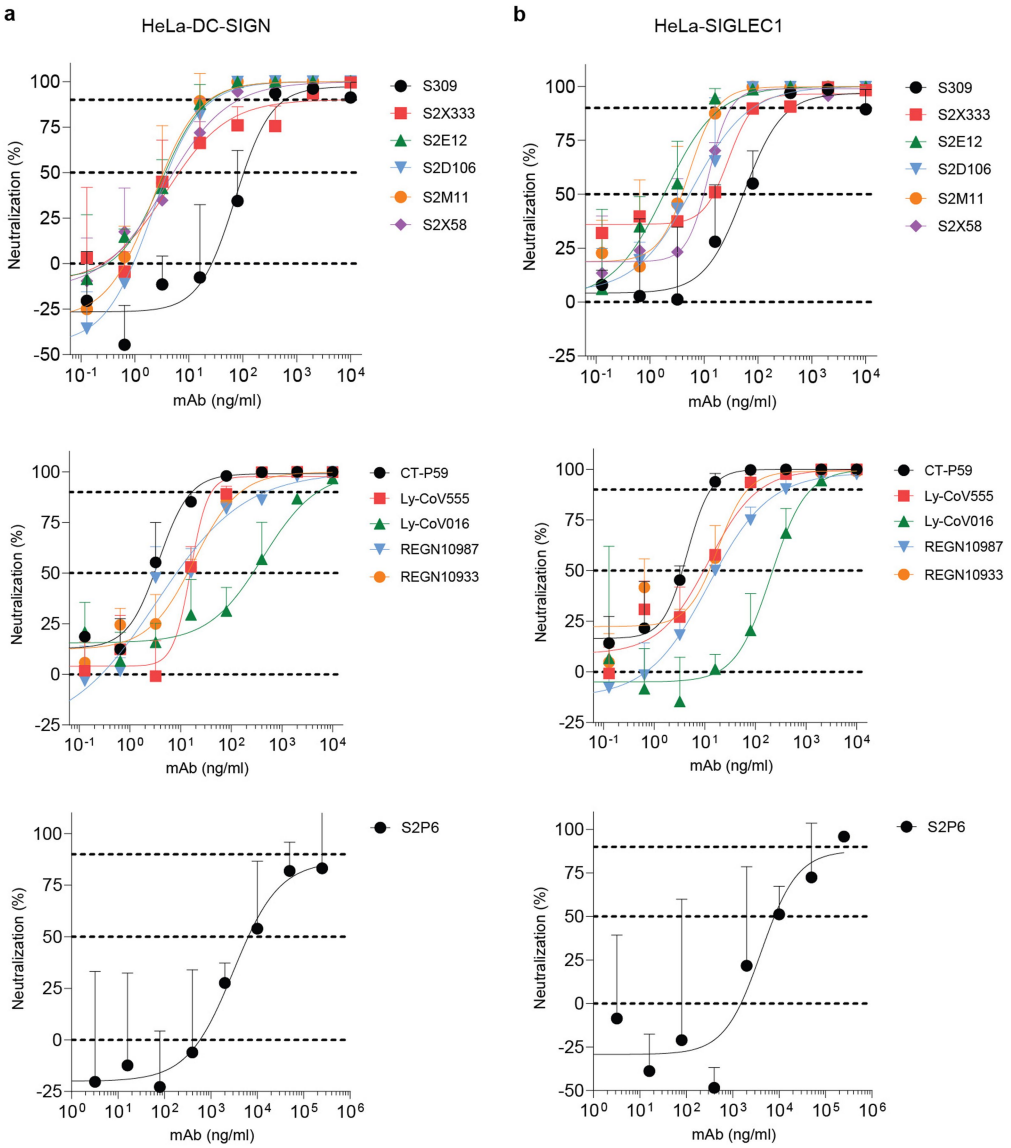

Extended Data Fig. 9 | Trans-infection neutralization. HeLa cells transduced with DC-SIGN (a) or SIGLEC1 (b) were incubated with VSV-SARS-CoV-2, extensively washed and incubated with serial dilutions of anti-spike antibodies. After 30 min, susceptible target cells (Vero-E6-TMPRSS2) were added for co-culture. Luminescence signal was quantified 24h post co-culturing to determine trans-infection levels ($n = 3$ biologically independent replicates).

Extended Data Table 1 | mAbs used in this study

mAb	Alias or derived mAb(s)	Domain (site)	ACE2 blocking	SARS-CoV	Phase	PDB	Ref
S309	VIR-7831 sotrovimab	RBD (IV)	-	+	EUA	7IX3	25
S2E12		RBD (Ia)	+	-	preclinical	7K4N	7
S2M11		RBD (Ib-lock)	+	-	preclinical	7K43	7
S2P6		S2 (stem helix)	-	+	preclinical	7RNJ	33
S2X58		RBD (Ib)	+	-	preclinical	this study	34
S2D106		RBD (Ia)	+	-	preclinical	7R7N	34
S2X259		RBD (IIa)	+	-	preclinical	7RA8	65
S2X333		NTD (i)	-	-	preclinical	7LXW,7LXY	26
Ly-CoV016	CB6/etesevimab	RBD (Ia)	+	-	EUA	7C01	66
Ly-CoV555	bamlanivimab	RBD (Ib)	+	-	EUA	7KMG	67,68
REGN10933	casirivimab	RBD (Ia)	+	-	EUA	6XDG	8,10
REGN10987	imdevimab	RBD (Ib)	+	-	EUA	6XDG	8,10
CT-P59	regdanvimab	RBD (Ia)	+	-	EUA	7CM4	69

*, SK, South Korea

nature research

Corresponding author(s): Amalio Telenti, Davide Corti

Last updated by author(s): Aug 6, 2021

Reporting Summary

Nature Research wishes to improve the reproducibility of the work that we publish. This form provides structure for consistency and transparency in reporting. For further information on Nature Research policies, see our Editorial Policies and the Editorial Policy Checklist.

Statistics

For all statistical analyses, confirm that the following items are present in the figure legend, table legend, main text, or Methods section.

n/a	Confirmed	
☐	☒	The exact sample size (*n*) for each experimental group/condition, given as a discrete number and unit of measurement
☒	☐	A statement on whether measurements were taken from distinct samples or whether the same sample was measured repeatedly
☐	☒	The statistical test(s) used AND whether they are one- or two-sided *Only common tests should be described solely by name; describe more complex techniques in the Methods section.*
☒	☐	A description of all covariates tested
☒	☐	A description of any assumptions or corrections, such as tests of normality and adjustment for multiple comparisons
☐	☒	A full description of the statistical parameters including central tendency (e.g. means) or other basic estimates (e.g. regression coefficient) AND variation (e.g. standard deviation) or associated estimates of uncertainty (e.g. confidence intervals)
☐	☒	For null hypothesis testing, the test statistic (e.g. *F*, *t*, *r*) with confidence intervals, effect sizes, degrees of freedom and *P* value noted *Give P values as exact values whenever suitable.*
☒	☐	For Bayesian analysis, information on the choice of priors and Markov chain Monte Carlo settings
☒	☐	For hierarchical and complex designs, identification of the appropriate level for tests and full reporting of outcomes
☐	☒	Estimates of effect sizes (e.g. Cohen's *d*, Pearson's *r*), indicating how they were calculated

Our web collection on statistics for biologists contains articles on many of the points above.

Software and code

Policy information about availability of computer code

Data collection	Perkin-Elmer Kaleido 3.0 Biotek Gen5 3.08 Perkin-Elmer Nivo 3.0.2
Data analysis	GraphPad Prism 9 was used to perform statistical analyses. R 4.0.2 (for figure 2a, b, c) (R packages: viridis_0.5.1, RColorBrewer_1.1-2, scales_1.1.1, cowplot_1.1.1, data.table_1.13.6, scater_1.16.2, ggplot2_3.3.3, SingleCellExperiment_1.10.1) NCBI Magic-BLAST 1.5.0 samtools 1.9 UCSF ChimeraX 1.1.1, Coot 0.8.9.2, BD FlowJo 10.7.1

For manuscripts utilizing custom algorithms or software that are central to the research but not yet described in published literature, software must be made available to editors and reviewers. We strongly encourage code deposition in a community repository (e.g. GitHub). See the Nature Research guidelines for submitting code & software for further information.

Data

Policy information about availability of data

All manuscripts must include a data availability statement. This statement should provide the following information, where applicable:

- Accession codes, unique identifiers, or web links for publicly available datasets
- A list of figures that have associated raw data
- A description of any restrictions on data availability

Source data associated with hamster experiments are included as source data provided with the manuscript. FACS gating strategies are provided as supplementary

information. The cryoEM maps have been deposited to the electron microscopy data bank with accession numbers EMD-24607 (2 RBDs open) and EMD-24608 (3 RBDs open). Single cell transcriptome datasets used in this study had been published previously: NCBI GEO (ID: GSE158055), NCBI SRA (ID: PRJNA608742). All further relevant source data that support the findings of this study are available from the corresponding author upon reasonable request.

Field-specific reporting

Please select the one below that is the best fit for your research. If you are not sure, read the appropriate sections before making your selection.

☒ Life sciences ☐ Behavioural & social sciences ☐ Ecological, evolutionary & environmental sciences

For a reference copy of the document with all sections, see nature.com/documents/nr-reporting-summary-flat.pdf

Life sciences study design

All studies must disclose on these points even when the disclosure is negative.

Sample size	Sample size = 6 was dimensioned in order to have a significant difference of at least 1 log viral RNA (Effect Size d = 2.004) between control and treated groups, by using a 2-tail T test with 80% power and an alpha error of 0.05, calculated with G*Power 3.1 software
Data exclusions	No data was excluded in vitro. In vivo, no data was excluded in control groups. In treated groups, animal with undetectable levels of circulating antibodies measured before infection were excluded, as this indicated a technical failure of drug administration.
Replication	Experimental assays were performed in biological duplicate or triplicate (or more) according to or exceeding standards in the field. We conducted all neutralization and antibody functional assays in biological duplicate, triplicate, or more, as indicated in relevant figure legends. In all cases, representative figure displays were appropriately replicated. In vivo data in Extended fig 4 are at least from two independent successful experiments (see the excel data source for the details). One group only (0.1 mg/kg) was tested once.
Randomization	Hamsters were allocated into different mAb/dosing groups at random.
Blinding	Blinding was performed: the samples for RNA and virus titration were run by the technicians blindly, without knowing the treatment group

Reporting for specific materials, systems and methods

We require information from authors about some types of materials, experimental systems and methods used in many studies. Here, indicate whether each material, system or method listed is relevant to your study. If you are not sure if a list item applies to your research, read the appropriate section before selecting a response.

Materials & experimental systems

n/a	Involved in the study
☐	☒ Antibodies
☐	☒ Eukaryotic cell lines
☒	☐ Palaeontology and archaeology
☐	☒ Animals and other organisms
☒	☐ Human research participants
☒	☐ Clinical data
☒	☐ Dual use research of concern

Methods

n/a	Involved in the study
☒	☐ ChIP-seq
☐	☒ Flow cytometry
☒	☐ MRI-based neuroimaging

Antibodies

Antibodies used	Human mAbs (all expressed & purified by Vir Biotechnology as part of this study): S309, S2E12, S2X333, S2M11, S2X58, S2D106, Ly-CoV016, CT-P59, Ly-CoV555, S2P6, S2X259, REGN10987, REGN10933 Primary Abs: rabbit-anti-SARS-CoV2-NC (Sino Biological, 40143-R001), mouse-anti-DC-SIGN/L-SIGN (Biolegend 845002), rabbit-anti-DC-SIGN (Cell Signaling, 13193S), mouse-anti-SIGLEC1 (Biolegend, 346002; Abcam, ab199401), goat-anti-ACE2 (R&D Systems, AF933), mouse-anti-VSV-G (clone 8G5F11, Absolute Antibody) Secondary Abs: goat-anti-mouse-AlexaFluor647 (Invitrogen, A32728), goat-anti-rabbit-AlexaFluor647 (Invitrogen, A21245), donkey-anti-goat-AlexaFluor647 (Invitrogen, A21447) Monoclonal antibodies (S309, S2E12, S2X333, S2D106, S2M11, S2X58, CT-P59, Ly-CoV555, Ly-CoV016, REGN10987, REGN10933) were produced in-house using recombinant protein purification as described in the Methods.
Validation	All SARS-CoV-2-spike specific antibodies have been described and validated in previous publications (Pinto et al., Nature, 2020; Tortorici et al., Science, 2021; Starr et al., Nature, 2021). Reactivity of primary antibodies listed above is based on the information on manufacturer's homepages.

Eukaryotic cell lines

Policy information about cell lines

Cell line source(s)	HeLa (ATCC, CCL-2), Vero E6 (ATCC, CRL-1586), MRC-5 (Sigma-Aldrich, 05072101-1VL), Lenti-X HEK293T cells (Takara, 632180), A549 (ATCC, CCL-185), HuH7 (Creative Bioarray, CSC-C9441L), CHO-K1 (ATCC, CCL-61), HEK293 Freestyle (Thermo Fisher Scientific, R79007)
Authentication	These cell lines were obtained from vendors that sell authenticated cell lines, they grew, performed and showed morphology as expected. No additional specific authentication was performed.
Mycoplasma contamination	Cell lines are routinely tested and tested negative for mycoplasma.
Commonly misidentified lines (See ICLAC register)	No commonly misidentified cell lines were used in this study.

Animals and other organisms

Policy information about studies involving animals; ARRIVE guidelines recommended for reporting animal research

Laboratory animals	Wild-type Syrian Golden hamsters (Mesocricetus auratus, female, 6-8 weeks of age) were purchased from Janvier Laboratories and were housed per two in ventilated isolator cages (IsoCage N Biocontainment System, Tecniplast) with ad libitum access to food and water and cage enrichment (wood block). The animals were acclimated for 4 days prior to study start.
Wild animals	No wild animals were used in this study.
Field-collected samples	No field-collected samples were used in this study.
Ethics oversight	Live virus-related work in hamsters was conducted in the high-containment ABSL3 and BSL3+ facilities of the KU Leuven Rega Institute (3CAPS) under licenses AMV 30112018 SBB 219 2018 0892 and AMV 23102017 SBB 219 20170589 according to institutional guidelines. Experimental procedures were approved by the ethics committee of animal experimentation of KU Leuven (license P065-2020)

Note that full information on the approval of the study protocol must also be provided in the manuscript.

Flow Cytometry

Plots

Confirm that:

☒ The axis labels state the marker and fluorochrome used (e.g. CD4-FITC).

☒ The axis scales are clearly visible. Include numbers along axes only for bottom left plot of group (a 'group' is an analysis of identical markers).

☒ All plots are contour plots with outliers or pseudocolor plots.

☒ A numerical value for number of cells or percentage (with statistics) is provided.

Methodology

Sample preparation	Cell lines were detached using TrypLE reagent and stained in suspension.
Instrument	Beckman-Coulter Cytoflex LX
Software	BD FlowJo software v10.7.1
Cell population abundance	Not applicable as homogenous cell lines were used for analysis.
Gating strategy	Gating on live cells was performed using FSC and SSC as outlined in the gating strategies.

☒ Tick this box to confirm that a figure exemplifying the gating strategy is provided in the Supplementary Information.